FRONTIERS OF PHYSICS

TOPICAL REVIEW
Volume 19 / Issue 2 / 23401 / 2024

Progress in the preparation and physical properties of two-dimensional Cr-based chalcogenide materials and heterojunctions

Xiulian Fan[1], Ruifeng Xin[1], Li Li[2,3], Bo Zhang[4], Cheng Li[1], Xilong Zhou[1], Huanzhi Chen[1], Hongyan Zhang[4], Fangping OuYang[1,4,5], Yu Zhou[1,5,†]

1 School of Physics and Electronics, Hunan Key Laboratory of Nanophotonics and Devices, Central South University, Changsha 410083, China
2 Jincheng Research Institute of Opto-mechatronics Industry, Jincheng 048000, China
3 Shanxi Key Laboratory of Advanced Semiconductor Optoelectronic Devices and Integrated Systems, Jincheng 048000, China
4 School of Physical Science and Technology, Xinjiang University, Urumqi 830046, China
5 State Key Laboratory of Powder Metallurgy, Central South University, Changsha 410083, China
Corresponding author. E-mail: †yu.zhou@csu.edu.cn
Received August 2, 2023; accepted August 23, 2023

ABSTRACT

Two-dimensional transition metal dichalcogenides (TMDs) exhibit promising application prospects in the domains of electronic devices, optoelectronic devices and spintronic devices due to their distinctive energy band structures and spin–orbit coupling properties. Cr-based chalcogenides with narrow or even zero bandgap, covering from semiconductors to metallic materials, have considerable potential for wide-band photodetection and two-dimensional magnetism. Currently, the preparation of 2D CrX_n (X = S, Se, Te) nanosheets primarily relies on chemical vapor deposition (CVD) and molecule beam epitaxy (MBE), which enable the production of high-quality large-area materials. This review article focuses on recent progress of 2D Cr-based chalcogenides, including unique crystal structure of the CrX_n system, phase-controlled synthesis, and heterojunction construction. Furthermore, a detailed introduction of room-temperature ferromagnetism and electrical/optoelectronic properties of 2D CrX_n is presented. Ultimately, this paper summarizes the challenges associated with utilizing 2D Cr-based chalcogenides in preparation strategies, optoelectronics devices, and spintronic devices while providing further insights.

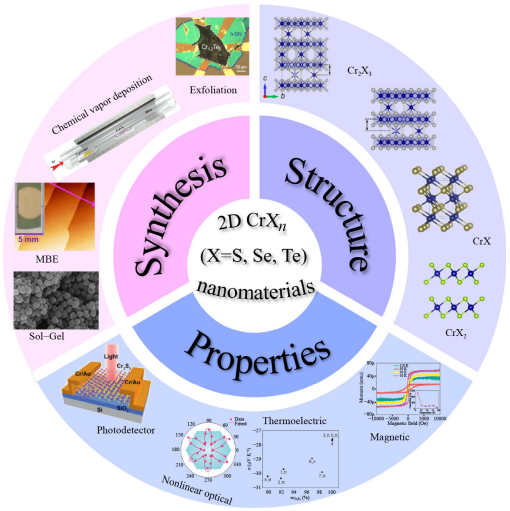

Keywords physical properties, two-dimensional materials, Cr-based chalcogenide, controlled synthesis, heterojunction, eletronic and optoelectronic devices

*Special Topic: Two-dimensional Materials for Optoelectronics (Eds.: Tianyou Zhai & Xing Zhou).

Higher Education Press

https://doi.org/10.1007/s11467-023-1342-y

Contents

1 Introduction

Recently, two-dimensional (2D) materials such as graphene, transition metal dichalcogenides (TMDs), and hexagonal boron nitride (*h*-BN) have demonstrated excellent mobility, chemical stability, suitable bandgap, and thermal conductivity [1–9]. These properties make them highly advantageous in field-effect transistors, photodetectors, and sensors [10–14]. In particularly, TMDs such as MoS_2 exhibit layer-dependent energy band structures with tunable bandgap and span a wide range of material systems from metallic, semi-metallic to semiconducting. This wide range of tunable bandgap, presents promising applications in photodetectors for detecting light across ultraviolet, visible and even infrared wavebands [15–19]. Additionally, the high mobility, surface flatness and atomic layer thickness of TMDs make them ideal candidates for electronic devices in the post-Moore era [20–22]. Furthermore, the unique electronic structures including strong electronic interactions and spin−orbit coupling effects of TMDs, provide opportunities for exploring 2D spintronics [23–27]. However, there are still certain limitations in the regulation of properties pertaining to monolayer TMDs materials. Currently, through the realization of 2D heterojunction electronic device fabrication, the application range of 2D materials can be significantly expanded, leading to the emergence of novel properties such as distinctive interlayer excitons and ultrafast charge transfer [28–30].

Since 2017, the discovery of 2D CrI_3, $Cr_2Ge_2Te_6$, and other 2D materials has initiated extensive research on single-layer 2D magnetic materials [31–33]. The presence of magnetic anisotropy enables the possibility of 2D magnetism possible, and while the search for 2D ferromagnetic materials with room-temperature Curie temperatures (T_C) has become a major focus of research objectives in the field [34–38]. The Cr-X (X = S, Se, Te) chalcogenides exhibiting NiAs-type structures have predominantly been studied in bulk form, and the diverse crystal phases of such materials contribute to their rich magnetic, thermoelectric, and optoelectronic properties [39–43]. The Cr-X system has a CrX_2 skeleton structure, in which the diverse phases are formed through the intercalation of Cr atoms between the different layers [44]. Among these compounds, semiconducting properties are observed in CrS and Cr_2S_3, while most other compounds exhibit semi-metallic or metallic behavior [45]. Most phase structures display ferromagnetic or antiferromagnetic properties, even exhibiting Curie temperatures at room temperature. The current research on 2D Cr-X materials focuses on the electrical and optoelectronic properties of Cr-S, the 2D magnetic and thermoelectric properties of Cr-Se, the magnetic behavior of Cr-Te, and the construction of various types of heterojunctions [46–51]. Furthermore, unlike conventional layered 2D materials, most of the CrX_n systems exhibit a non-layered three-dimensional structure. Achieving controlled synthesis of such non-layered materials in 2D limited thickness remains a crucial area for further investigation [52–55]. Therefore, a comprehensive overview of the current synthesis methods and intrinsic material properties of non-layered 2D Cr-based chalco-

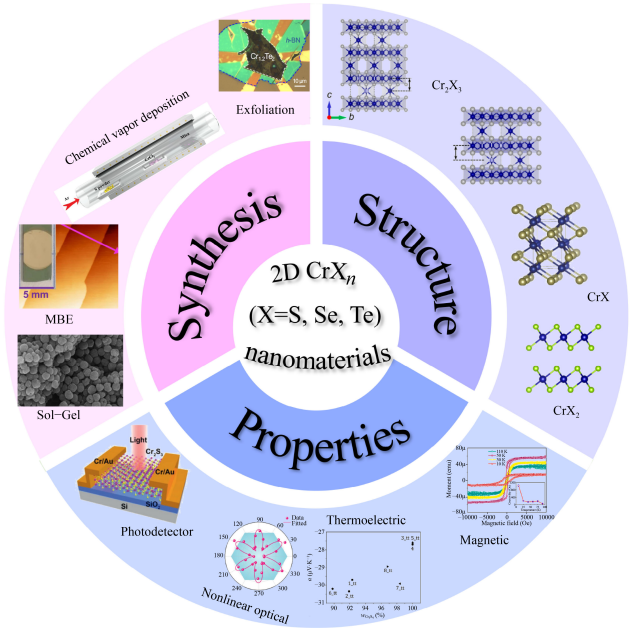

Fig. 1 A comprehensive review on the structure, synthesis, and emerging physical properties of two-dimensional Cr-based chalcogenides.

genides is significant for guiding their application in future spintronic and optoelectronic devices.

In this review, we present a comprehensive summary of the crystal structure, synthetic methods, and physical properties of 2D CrX_n, as shown in Fig. 1. Firstly, a variety of CrX_n phase structures resulting from different Cr atoms intercalation in layered CrX_2 materials are discussed. Secondly, we introduce the preparation of CrX_n for these 2D layered and non-layered structures, and highlight the challenge of achieving precise control over the CrX_n phases through CVD. We also summarize the preparation and theoretical study of heterojunctions based on 2D nanosheets of CrX_n. Additionally, we emphasize on room-temperature ferromagnetism of 2D CrX_n including magnetic anisotropy properties, magnetic phase transition behavior and strain-induced magnetic modulation effects. Finally, we introduce electrical and optoelectronic properties associated with semiconductor-like behavior observed in Cr_2S_3 as well as device applications for 2D CrX_n.

2 Development and structure of 2D Cr-based chalcogenides

2.1 Two-dimensional magnetic materials

Previously, according to the Mermin-Wagner theorem [56], 2D spin-ordered terms cannot be formed due to thermal fluctuation at non-zero temperature. And thus, no two-dimensional long-range magnetic order exists. However, the existence of magnetic anisotropy could break this limitation. In 2017, Zhang *et al.* [32] and Xu *et al.* [31] demonstrated the existence of intrinsic ferromagnetism in two-dimensional conditions for $Cr_2Ge_2Te_6$ (Heisenberg magnetic anisotropy) and CrI_3 (2D Ising model), respectively, which has raised the research frenzy of 2D magnetic materials since then. As shown in Fig. 2(a), Xu *et al.* [31] used the mechanical exfoliation method to exfoliate the van der Waals layered CrI_3 single-crystal bulk to monolayer, and found that even the monolayers of CrI_3 still have obvious hysteresis with the measurement of magneto-optical Kerr measurements (MOKE), which exhibit out-of-plane spin polarization properties. Moreover, the ferromagnetic behavior of CrI_3 has obvious layer-dependent properties, showing that monolayer CrI_3 is ferromagnetic, bilayer CrI_3 is antiferromagnetic, and trilayer and bulk CrI_3 transform to ferromagnetic again. Meanwhile, as shown in Fig. 2(b), Zhang *et al.* [32] investigated the temperature-dependent magnetism of mechanically exfoliated bilayers of $Cr_2Ge_2Te_6$ under a 0.075 T vertical field. As the temperature decreases, bilayer $Cr_2Ge_2Te_6$ nanoflakes exhibited significant ferromagnetism at non-zero temperature, that is, the existence of 2D ferromagnetic ordering. After that, a series of typical intrinsic ferromagnetic 2D materials have been found due to the presence of magnetic anisotropy.

For example, the more extensively studied van der Waals 2D Fe_3GeTe_2 (FGT) material, whose structure is shown in Fig. 2(c), was obtained as a monolayer FGT sample from a bulk single crystal using the Al_2O_3-assisted exfoliation method [33]. Obviously, the T_C of FGT samples significantly decreased from 180 K in the bulk to 20 K in the monolayer. They also found that the T_C of the FGT materials could be improved by doping. The doping mentioned here is electron doping, through the positive gate voltage to insert lithium ions into the FGT nanosheets, resulting in a certain degree of electron doping. This kind of ion gate induced electron doping can significantly affect the electronic band of FGT, resulting in the change of DOS at the Fermi level and the obvious regulation of ferromagnetism. The interesting intrinsic ferromagnetism and spin properties of these 2D magnetic materials have attracted widespread attention of physicists and further enriched the development of the family of 2D materials. In recent years, the 2D magnetic materials represented by Cr-based chalcogenides (CrX_n, X = S, Se, Te) have made great development, and this large class of materials contains both layered and nonlayered, with unique characteristics of narrow band gap, ferromagnetism, and thermoelectric properties [40, 45, 58]. The calculated electronic band structure of Cr_2X_3 (X = S, Se, Te) is shown in Fig. 2(d). It is evident that Cr_2S_3 is a typical narrow band gap semiconductor structure (E_g ~ 0.45 eV), Cr_2Se_3 has semimetallic and semiconductor properties at different symmetry points (E_g ~ 0.034 eV), and Cr_2Te_3 exhibits

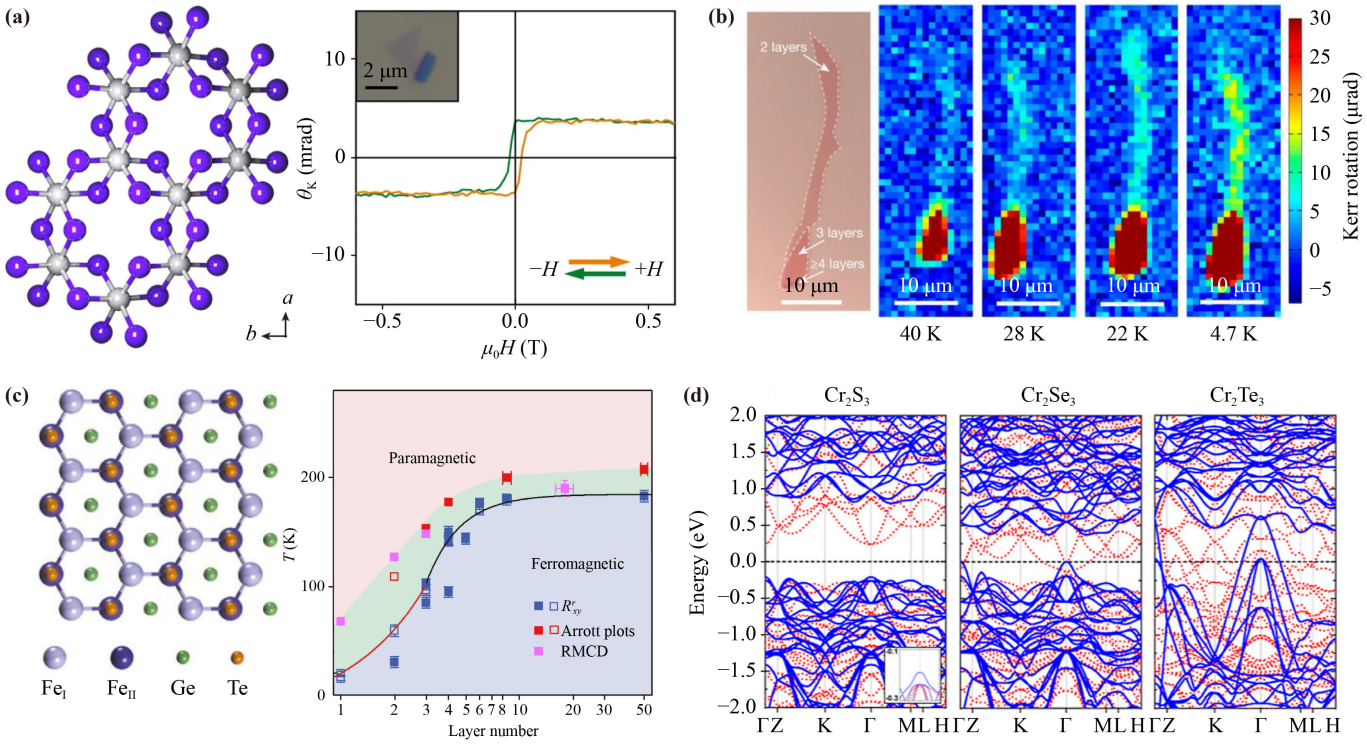

Fig. 2 Structure and magnetic properties of 2D magnetic materials. **(a)** Crystal structure and MOKE measurement of CrI_3 single layer [31]. **(b)** Optical morphology and temperature-dependent Kerr rotation of bilayer $Cr_2Ge_2Te_6$ [32]. **(c)** Atomic structure and layer-dependent variation of ferromagnetic phase diagram of monolayer Fe_3GeTe_2 [33]. **(d)** The electronic band structures of Cr_2S_3, Cr_2Se_3 and Cr_2Te_3 [57].

obvious metallicity [57]. Furthermore, the spin-selective tuning of the band gap and the induced magnetic phase transition can be achieved under strain modulation.

2.2 Atomic structures of the stoichiometric ratio of CrX_n

The atomic structures of CrX_n are generally formed by alternating stacks of Cr-rich and Cr-poor atomic layers filled in the X_6 octahedron, in which the different filling ability of Cr atoms results in the phase diversity of CrX_n including layered CrX_2 and other non-layered structures. By utilizing the particle swarm optimization algorithm in conjunction with first-principles calculations, Liu *et al.* [59] identified several possible crystal structures of CrTe, as illustrated in Fig. 3(a). These crystal configurations include the unstable *Cmca* and $R\bar{3}m$ structures, as well as the experimentally prepared ground-state $P6_3/mmc$ structure [60]. Under high pressures of 34 and 42 GPa, CrTe undergoes phase transformations to $R\bar{3}m$ and $Fm\bar{3}m$ phases from its ground state. In addition to CrTe, a stable phase of CrSe has also been successfully prepared in the experiment among the Cr-based chalcogenides. This non-layered material exhibits typical 2D ferromagnetic properties and shares the same space group $P6_3/mmc$ as the ground state of CrTe [61].

Currently, the experimentally synthesized 2D Cr-S nanomaterials mainly consist of van der Waals layered CrS_2 [64] and non-layered Cr_2S_3 [53, 65]. These two compounds also exhibit multiple phase states. Figure 3(b) presents the monolayer atomic structures of layered CrS_2 in different phases. The generalized gradient approximation (GGA) function was utilized to calculate the relative formation energies of these three structures with 2H-CrS_2 as a reference. The calculated values for the relative formation energy per CrS_2 unit are 0.521 and 0.37 eV for 1T and 1T'-CrS_2, respectively. Meanwhile, the Perdew-Burke and Ernzerhof (PBE) function theoretically predicts the band gap, revealing that 2H-CrS_2 possesses a band gap of approximately 0.95 eV, while 1T-CrS_2 and 1T'-CrS_2 exhibit metallic and semimetallic properties with a band gap size of around 10 meV, respectively [62]. For Cr_2S_3, there exist two primary stable phases, the trigonal and rhombohedral phases [66, 67]. Both of them are semiconductive properties, with a theoretically predicted band gap of 0.45 eV for rhombohedral Cr_2S_3 [45]. The key to distinguish two structures is the stacking arrangement of the $Cr_{1/3}S$ layer and the CrS layer. The crystal structures of Cr_2S_3 in various phases and the newly predicted relatively unstable γ-Cr_2S_3 are illustrated in Fig. 3(c) [63]. Firstly, it is obvious that α-Cr_2S_3 is a rhombohedral $R\bar{3}$ structure with an "ABCABC..." stacking sequence, while β-Cr_2S_3 exhibits a trigonal $P\bar{3}1c$ structure with an "ABAB..."

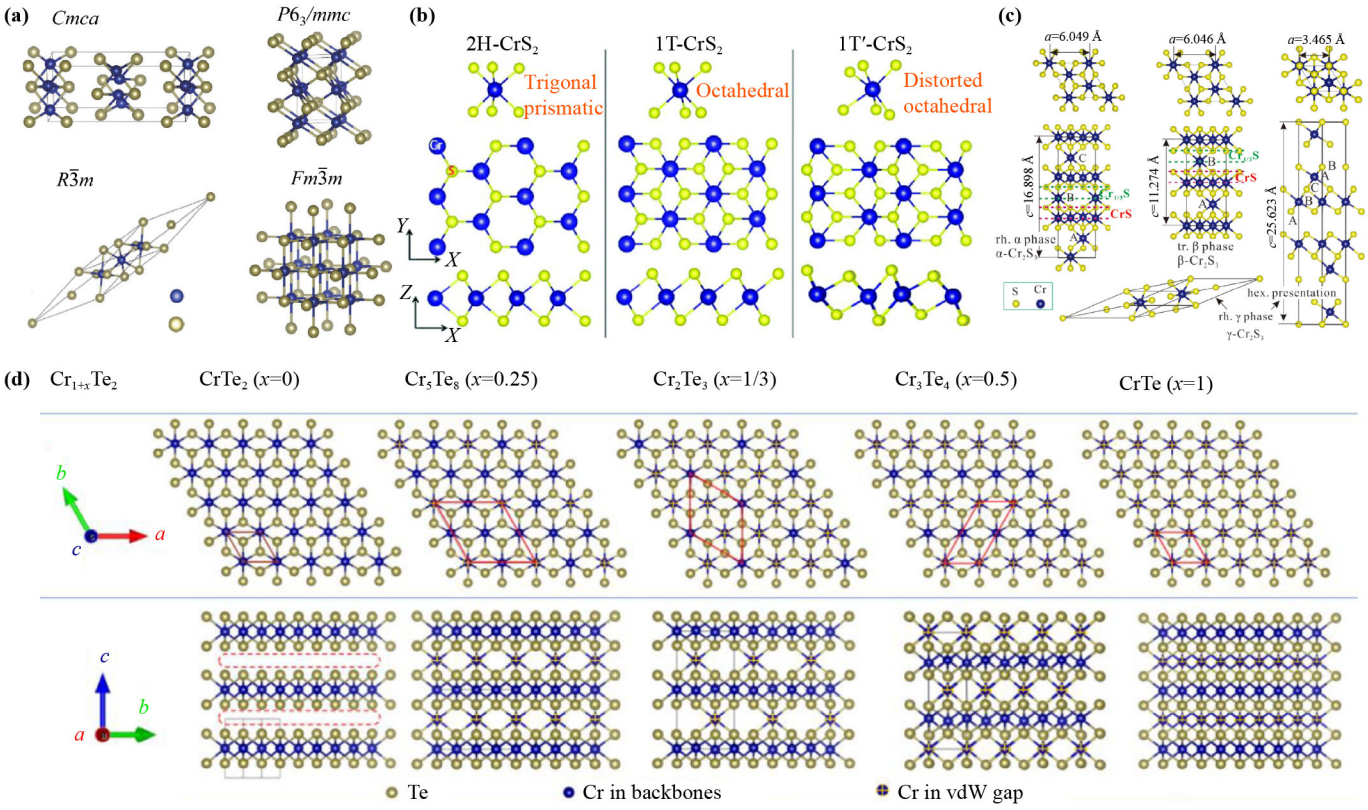

Fig. 3 Typical CrX_n crystal structure for different atomic ratios. **(a)** Calculation of the theoretically predicted atomic structures of different space groups of CrTe: *Cmca*, $P6_3/mmc$, $R\bar{3}m$ and $Fm\bar{3}m$ [59]. **(b)** Top and side views of the atomic structure of CrS_2 in the 2H, 1T and 1T' phase [62]. **(c)** Atomic structures of air-stable α-Cr_2S_3, β-Cr_2S_3 and theoretically predicted metastable phase γ-Cr_2S_3 [63]. **(d)** Crystal structure of $Cr_{1+x}Te_2$ formed by different Cr atom intercalation filling rates [51].

arrangement. Both two phases are typical non-van der Waals crystal structures, wherein each atom forms covalent bonds in three-dimensional space. In contrast, the novel predicted structure of γ-Cr_2S_3 is linked along the [111] direction by van der Waals forces in an "ABCAB..." stacking mode. The indirect band gap increases from 1.23 eV in bulk material to 1.97 eV in a single layer of γ-Cr_2S_3 according to HSE06 calculation. So far, the crystal structure of Cr-Se system is relatively simple, mainly including $P6_3/mmc$ CrSe [61], 1T-$CrSe_2$, 2H-$CrSe_2$, $P\bar{3}m1$ Cr_3Se_4, trigonal Cr_2Se_3 and rhombohedral Cr_2Se_3. Similarly, only $CrSe_2$ is a vdW layered material, while the rest remain unlayered and have a crystal structure similar to that of the Cr-S system. Sawa *et al.* [68] synthesized 1T-$CrSe_2$ with a $P\bar{3}m1$ space group structure. Tankeshwar *et al.* [42] calculated the band structure of 2H-$CrSe_2$, whose space group is $P\bar{6}m2$, from the bulk material to single-layer $CrSe_2$, whose band gap changes from an indirect band gap of 0.56 eV to a direct band gap of 0.75 eV. Using first-principles calculations, Ma *et al.* [27] concluded that the single-layer Cr_2Se_3 space group is $P\bar{6}m2$ and also demonstrated that the single-layer Cr_2Se_3 is a valleytronic semiconductor with an indirect band gap of 0.57 eV. The Cr_2Se_3 nanosheets synthesized by Zhou and Wang *et al.* [69, 70] all have a rhombohedral structure with $R\bar{3}$.

In terms of the diversity of phases, the Cr-Te system among Cr-based chalcogenides exhibits greater complexity than the Cr-S and Cr-Se compounds. Figure 3(d) displays the top and side views of several typical structures for stoichiometric $Cr_{1+x}Te$ crystals [51]. As previously discussed, the wide range of atomic structure ratios in Cr-based chalcogenides can be attributed to the filling densities of the Cr-filled layers. Only $CrTe_2$ is a van der Waals layered material, while different levels of Cr atom filling between the two Te-Cr-Te atomic layers can lead to stable non-layered Cr-Te compounds with various ratios. At present, the synthesized $CrTe_2$ includes 1T phase with a space group of $P\bar{3}m1$ and 2H phase with $P3m1$ [23, 71]. The monolayer 1T-$CrTe_2$ is composed of Cr atoms containing Te octahedral vacancies, and the interlayers are held together by van der Waals forces. The insertion of a specific number of Cr atoms into the van der Waals gap between two layers of 1T-$CrTe_2$ can result in the formation of various phases [44, 51, 72], such as the trigonal and monoclinic Cr_5Te_8 structures formed by $Cr_{1/4}Te$ and CrTe [73], $Cr_{1/3}Te$ and CrTe overlapping Cr_2Te_3 with a space group of $P\bar{3}1c$ [74], $C2/m$ space group structured Cr_3Te_4 formed by $Cr_{1/2}Te$ and

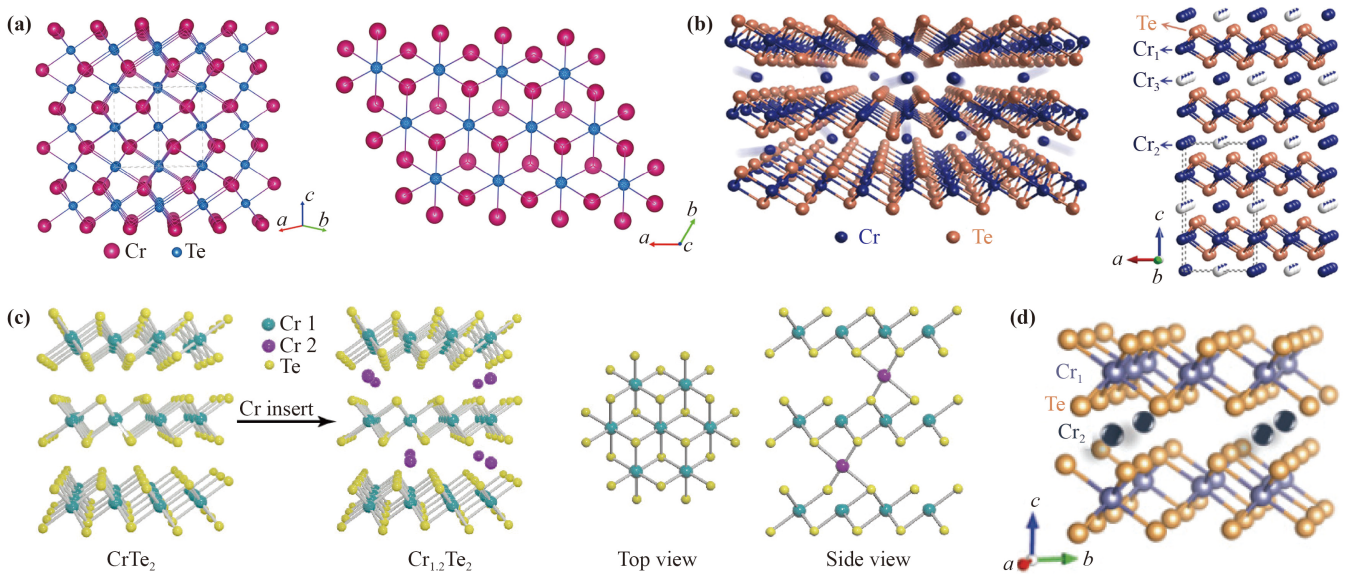

Fig. 4 Crystal structure of the non-stoichiometric ratio $Cr_{1+x}Te_2$. **(a)** Top and side views of the crystal structures of CrTe [79]. **(b)** Schematic diagram of Cr intercalated $CrTe_2$ structure and side view of $Cr_{1.53}Te_2$ [37]. **(c)** Crystal structure of $Cr_{1.2}Te_2$ composed of Cr intercalated $CrTe_2$ van der Waals gap [80]. **(d)** Side view of the intercalated atomic structure of $Cr_{4.14}Te_8$ [81].

CrTe [75], and complete filling of the gap with Cr resulting in pure phase of CrTe. In addition, there are also various structures such as $CrTe_3$, Cr_4Te_5, and all of them present unique magnetic or electrical properties [76–78].

2.3 The atomic structure of non-stoichiometric ratios of $Cr_{1+x}Te_2$

As previously mentioned, this unique Cr intercalation behavior of $CrTe_2$ enables not only a variety of atomic ratios of $CrTe_n$, but also often a variety of non-stoichiometric ratios due to the experimentally controlled nature of the compounds. Figure 4(a) depicts the typical atomic structure of $P6_3/mmc$ CrTe. While wang *et al.* [79] successfully prepared a single crystal of $Cr_{0.87}Te$ with Cr vacancies through thermal annealing, demonstrating not only the ability to obtain specific ratios of intercalated $CrTe_n$ materials but also the possibility of synthesizing non-stoichiometric $Cr_{1+x}Te_2$ by introducing Cr defects. Figure 4(b) shows the crystal structure of $Cr_{1.53}Te_2$, which is composed of Cr atom intercalation and belongs to the monoclinic $C2/m$ space group, consistent with the structure of monoclinic Cr_3Te_4 [37]. Further decreasing the filling rate of Cr atoms in the van der Waals gap, a $Cr_{1.2}Te_2$ single crystal was prepared by Xiang *et al.* [80]. As depicted in Fig. 4(c), $Cr_{1.2}Te_2$ exhibits the same $P\bar{3}m1$ space structure similar as $CrTe_2$. Sun *et al.* [81] reported the discovery of a hexagonal $Cr_{4.14}Te_8$ single crystal with a $P\bar{3}m1$ structure as shown in Fig. 4(d), in which embedded Cr atoms are located within the van der Waals gap between the $CrTe_2$ layers, resulting in lattice distortion and alteration of the lattice constant. Based on these reports, it is obvious that all $Cr_{1+x}Te_2$ compounds with non-stoichiometric ratios have a crystal structure similar to that of the stoichiometric compounds. The observed different properties are mainly attributed to specific lattice distortions induced by the intercalation of Cr atoms or vacancies. From the aforementioned studies, it is evident that the key to the wide variety of phases in Cr-based chalcogenides can be identified, while it is particularly crucial to change the number of intercalated Cr vacancies through different synthesis methods to achieve the phase modulation of such multiphase materials. Moreover, the special properties of Cr-X compounds with various atomic ratios are also significant for their application in optoelectronic and spintronic devices.

3 Synthesis of 2D CrX_n nanomaterials

Cr-based chalcogenides systems comprise both layered materials, such as MoS_2 [21], WS_2 [82], and non-layered compounds. Achieving precise control over the thickness, phase, and size of 2D CrX_n nanosheets, whether they are layered or non-layered, has been a major research focus for investigating their physical properties and device applications. Various methods such as mechanical exfoliation, solution method, hydrothermal synthesis, molecular beam epitaxy and chemical or physical vapor deposition have been used to synthesize CrX_n nanomaterial systems. Among them, the chemical vapor deposition method has been extensively studied up to now.

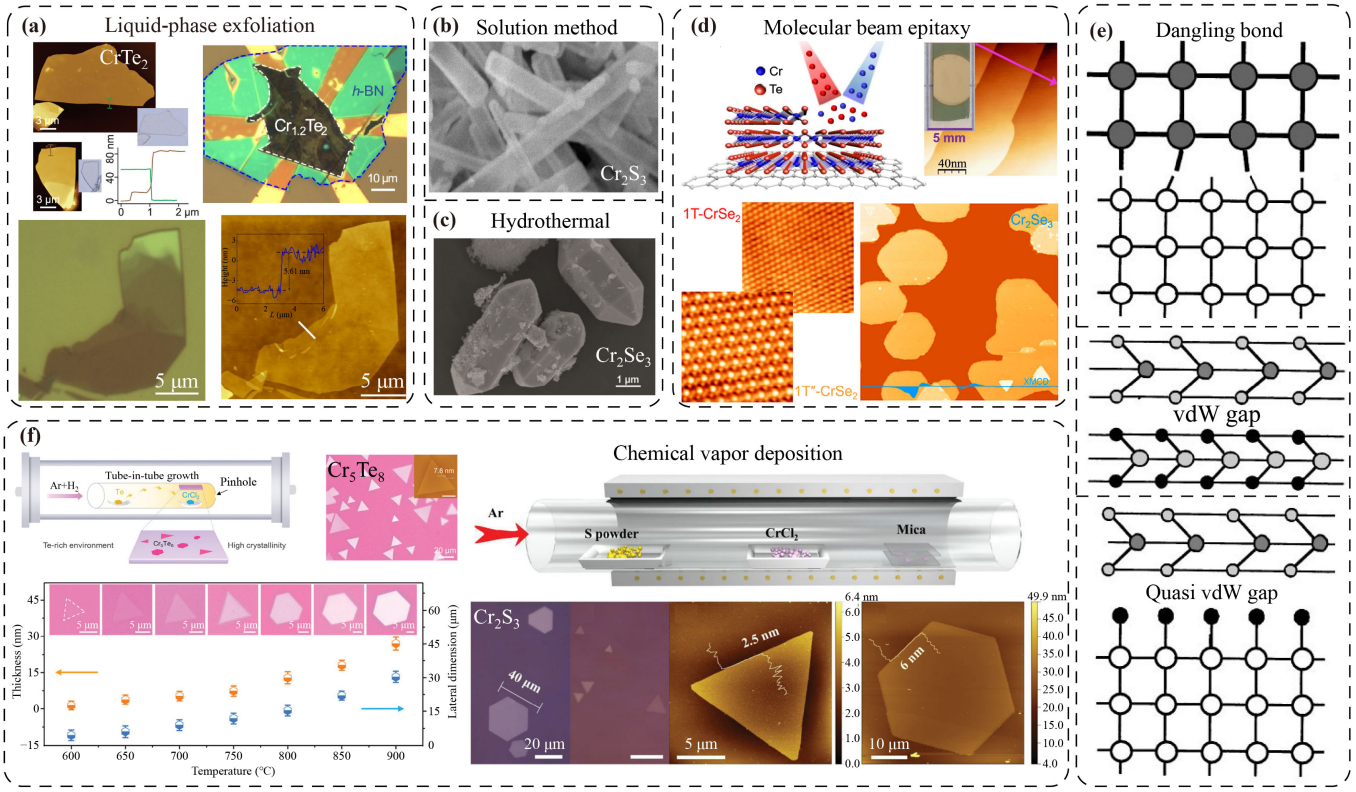

Fig. 5 The main preparation methods of Cr-based sulfur nanomaterials. **(a)** OM and AFM images of a few atomic layers of $Cr_{1.2}Te_2$ and $CrTe_2$ prepared by liquid-phase exfoliation method [73, 80]. **(b)** SEM image of Cr_2S_3 nanorods prepared by solution method [89]. **(c)** SEM image of hydrothermally synthesized *h*-Cr_2Se_3 nanosheets [90]. **(d)** Schematic diagram and STM topography image of $CrTe_2$ films synthesized on graphene by MBE (top) [91]; atomic-resolution STM images of 1T-$CrSe_2$ and 1T'-$CrSe_2$ and STM image of Cr_2Se_3 grown by MBE (bottom) [92]. **(e)** Schematic diagram of interface connection of dangling bond (top), van der Waals gap (middle) and quasi van der Waals gap (bottom) [93]. **(f)** Schematic diagram of improved CVD synthesis of 2D Cr_5Te_8 crystals and OM images of the grown Cr_5Te_8 nanosheets at different temperatures (left) [94]; schematic illustration of 2D Cr_2S_3 crystals by confined-space CVD, accompanied by OM and AFM images of Cr_2S_3 nanoflakes (right) [65].

3.1 Diverse preparation methods for two-dimensional CrX_n

3.1.1 Liquid phase exfoliation

Liquid-phase exfoliation is a widely used method for the preparation of 2D materials, in which chemical ion intercalation has been developed as an assisted liquid-phase exfoliation to obtain 2D MX_2 nanosheets. The most common method involves using compounds such as Li_xMX_2 or Na_xMX_2 to form dispersions in solvents, resulting in ultrathin dispersed MX_2 nanosheets after sonication [83–85]. As illustrated in Fig. 5(a), Coraux *et al.* [73] synthesized $KCrTe_2$ single crystal using a specific molar mixture of Cr, K, and Te at 1170 K for 8 days. Subsequently, the deintercalation of K ions was completed by reacting $KCrTe_2$ with an iodine solution in acetonitrile. Finally, the iodide was removed using acetonitrile followed by filtration and drying to obtain millimeter-sized flakes of $CrTe_2$. In a similar way, Xiang *et al.* [80] subjected the K, Cr, and Te mixture to a 900 °C heating process for 24 h and maintained it for 7 days to obtain $KCr_{1.2}Te_2$ single crystal. The grown crystal was then immersed in the solution of iodine in acetonitrile to achieve the deintercalation of K ions. Finally, $Cr_{1.2}Te_2$ was obtained by repeated washing in acetonitrile solution, filtering and drying. By this method, nanoflakes with a lowest thickness of 5.61 nm were obtained as shown in Fig. 5(a) (bottom). Obviously, the intercalation liquid phase exfoliation method is particularly common in the synthesis of 2D $CrTe_2$ flakes and can be easily prepared in large quantities [86–88]. But it is almost exclusively applicable to this class of layered structures, so other synthetic methods are needed for other Cr-based chalcogenides with non-layered phase structures.

3.1.2 Solution and hydrothermal synthesis methods

Solution based chemical synthesis methods are commonly used for preparing 2D thin films and nanostructures, offering the advantages such as large-scale

production, and controlled low-temperature reactions. Ali *et al.* [89] successfully synthesized low-dimensional Cr_2S_3 nanomaterials with different morphologies via chemical solution methods utilizing a single precursor source or a multi-source precursor, respectively. Firstly, a single precursor source of thiourea-chromium complex was synthesized by adding $CrCl{\cdot}6H_2O$, thiourea and acetone in a round bottom flask. Using thiourea-chromium complex as the reaction precursor source, it was dissolved in ethylene glycol and heated to 180 °C and kept overnight, and finally other by-products such as ethylene glycol were removed with methanol to obtain short rods of Cr_2S_3 as shown in Fig. 5(b) [89]. However, compared to the single source precursor, the multi-source precursor approach involves direct addition of thiourea and $CrCl_2{\cdot}6H_2O$ into an autoclave containing ethylene glycol. The resulting mixture is then subjected to overnight heating at 180 °C within a furnace before being washed with methanol to yield Cr_2S_3 nanoparticle. Obviously, different synthesis paths can significantly affect the morphology of Cr_2S_3. Jie *et al.* [95] have successfully synthesized sub-micron $CrSe_2$ flakes on Si (110) and glass substrates using a solvothermal method. 2 mmol of Se and Cr powder were introduced into 30 mL of ethylenediamine, followed by stirring for 10 min. The glass, Si (110) substrates and the mixture were put into an autoclave. The autoclave was maintained at 200 °C for two weeks before removing the substrate. After cleaning and drying with ethanol, the substrates were heated to 300 °C for 2 hours under an argon atmosphere to obtain $CrSe_2$ nanosheets. The synthesized low-dimensional $CrSe_2$ exhibited the sizes ranging from 5 to 15 μm and thicknesses around several hundred nanometers. Kariper *et al.* [96, 97] utilized chemical bath deposition to synthesize CrSe film. Hydrochloric acid, chromium nitrate, Se source solution and ethanolamine were employed as precursors. The substrate was immersed in the mixed bath at a certain pH and held at 50 °C for 3 hours. As shown in Fig. 5(c), Velusamy *et al.* [90] used chromium acetate and selenium as precursors to synthesize *h*-Cr_2Se_3 hexagonal sheets for the first time using a hydrothermal method. The high crystallinity of as-synthesized *h*-Cr_2Se_3 indicates that it is suitable for the preparation of high-quality metal-sulfide compounds. We anticipate that chemical solution-based synthesis and hydrothermal synthesis of 2D materials will have a significant influence on the future large-scale production and improved device application of two-dimensional Cr-based chalcogenides.

3.1.3 Molecular beam epitaxy

Molecular beam epitaxy (MBE) is the predominant technique utilized for the preparation of crystalline thin films, which has been extensively employed in the fabrication of condensed physics and diverse optoelectronic devices [98–100]. In recent years, the application of MBE in the preparation of CrX_n thin films has gained widespread attention due to the rapid development of ferromagnetic 2D Cr-based materials [43, 100, 101]. Figure 5(d) (top) illustrates the schematic and scanning tunneling microscope (STM) images of 2D $CrTe_2$ thin films [91]. The 1T-$CrTe_2$ films grown by MBE on bilayer graphene/SiC substrates at a deposition rate of 0.73 Å/min, using high-purity Cr and Te as the electron-beam evaporation source while maintaining the substrate temperature of 375 °C, exhibit the transverse dimension up to 5 mm. The STM topology image reveals that the grown 1T-$CrTe_2$ films possess a typical hexagonal lattice structure and demonstrate layer-by-layer growth patterns with atomic-level flatness. Moreover, Wang *et al.* [102] used the MBE method to epitaxially grow hexagonal Cr_2Te_3 films on Al_2O_3 substrates. The X-Ray diffraction (XRD) analysis of this film showed that it has a single [001] orientation and its *c*-axis lattice constant showed a slight increasing with the increased sample thickness. As shown in Fig. 5(d) (bottom), Wee *et al.* [92] synthesized monolayer $CrSe_2$ with the coexistence of 1T and 1T'' phases on HOPG substrates using MBE under ultra-high vacuum (10^{-9} mbar). From the atomic-resolution STM images, 1T-$CrSe_2$ exhibits hexagonal symmetry with a lattice spacing of (3.3 ± 0.1) Å and a 1 × 1 surface periodicity. While the distorted 1T''-$CrSe_2$ shows six asymmetric points around the brighter spots with a lattice spacing of (6.5 ± 0.1) Å and a 2 × 2 surface periodicity. Furthermore, upon annealing the monolayer of $CrSe_2$ at a temperature of 300 °C, the sample underwent a transformation into monolayer Cr_2Se_3 and displayed a thickness increasement from 0.8 nm to 1.1 nm. To overcome the defects in the Cr_2Se_3 samples, monolayer Cr_2Se_3 was synthesized directly on the HOPG substrate at 300 °C, in which the high-quality film with specific shapes shows a lattice spacing of (3.6 ± 1) Å under lower defect density. In short, the MBE growth is commonly used for high-quality 2D materials synthesis method for layered and nonlayered materials, which requires an extremely demanding growth environment, equipment and very clean substrates. The high-quality films via the MBE method are of utmost important for investigating the physical properties of 2D Cr-based chalcogenides and also plays a crucial role in the improved device performance of electronic and optoelectronic devices.

3.1.4 Chemical vapor deposition

Chemical vapor deposition (CVD), the most prevalent method for synthesizing 2D materials, involves the adsorption and diffusion of active precursors on a substrate surface, followed by a chemical reaction to produce solid products, and has enabled the preparation of a variety of 2D layered and nonlayered materials [52, 103, 104]. Among the Cr-based chalcogenides, only CrS_2, $CrSe_2$ and $CrTe_2$ exhibit typical layered materials in this

materials family, while the rest phases are non-layered materials with a significant number of unsaturated dangling bonds on the surface, which make it difficult to obtain 2D nanosheets or thin films with controllable thickness by conventional epitaxy methods. Considering the difficulty of epitaxial growth on substrates, many researchers have resorted to using epitaxial substrates in order to overcome lattice mismatch at the interface of materials. Figure 5(e) depicts a schematic diagram of interfacial bonding under three different kinds of epitaxial conditions [93]. In conventional epitaxial growth, the epitaxial material is chemically bonded to the substrate, and a strict lattice match between them is necessary to eliminate the problem of excessive stress caused by interfacial bonds. However, due to the diversity of materials, it is difficult to find a universal epitaxial substrate for all of materials. The proposed van der Waals epitaxial growth offers a practical solution to address this issue. As shown in Fig. 5(e) (middle) for the van der Waals epitaxial growth, the interface between the layered material and substrate is connected by weak van der Waals forces, in which the lattice mismatch could be relaxed up to 10% that the interface shows the negligible interfacial stress. This greatly enhances lattice mismatch tolerance and reduces material selectivity to the substrate. Subsequently, the van der Waals epitaxial growth technique was further developed to the quasi-van der Waals epitaxy, as shown in Fig. 5(e) (bottom). The quasi-van der Waals epitaxy refers to the process of growing layered materials on non-layered substrates or non-layered materials on layered substrates. This epitaxy also does not involve the formation of chemical bonds at the interface, but instead relies on weak van der Waals forces, which can greatly improve the tolerance of lattice mismatch. At present, most CVD growth of Cr-based chalcogenides is based on quasi-van der Waals epitaxial growth method and can achieve precise control over size, morphology, and thickness [55, 61, 105].

The schematic diagram and morphology of Cr_5Te_8 (left) and Cr_2S_3 (right) nanosheets prepared by CVD are illustrated in Fig. 5(f). Xu *et al.* [94] used a tube-in-tube CVD growth method to epitaxially synthesize Cr_5Te_8 nanosheets with high quality and controlled thickness on mica substrates, using $CrCl_2$ and Te as precursors. This method differs from conventional CVD, in which a small quartz tube (1.5 cm in diameter) is incorporated within the tube furnace quartz tube and is fully open at one end and only features a small 3 mm aperture at the other end. The utilization of such a growth strategy ensures a continuous and stable supply of Cr and Te precursor sources, thereby driving the reaction equilibrium towards the synthesis of high-quality Cr_5Te_8 nanosheets. In addition, a detailed investigation was conducted on the impact of growth temperature on the synthesis of Cr_5Te_8 nanosheets. The thickness and lateral size of the nanosheets increased from 1.2 to 26 nm and from 5 to 30 μm, respectively, as the temperature rose from 600 °C to 800 °C. Meanwhile, the morphology transformed from trigonal to hexagonal shapes. Moreover, this tube-in-tube CVD method is particularly effective in regulating the Cr_xTe_y components, and by adjusting the supplying quality of the precursors. This report showed the structures such as Cr_3Te_4 and $CrTe_2$ can be also obtained. This preparation technique produces 2D chromium chalcogenides nanosheets with high crystal quality and excellent air stability. The Cr_2S_3 nanosheets were epitaxially grown on the mica surface using a space-confined CVD method, as shown in Fig. 5(f) (right) [65]. Similarly, the use of $CrCl_2$ and powder S as precursors for Cr and S, respectively, in conjunction with two stacked mica sheets as growth substrates separated by a gap (less than 100 μm), serves to limit precursor supply and facilitates epitaxial growth of non-layered materials on mica surfaces. The thickness of Cr_2S_3 nanosheets was successfully reduced to 2.5 nm for the first time, while achieving a lateral size of up to 40 μm. Additionally, during the investigation of Cr_2S_3 growth on SiO_2/Si substrates, clear evidence of vertical nanosheet growth was observed, further confirming the previously mentioned inhibition of lateral growth in non-layered materials by surface dangling bonds. As an important preparation method for 2D materials, CVD growth stands as the most promising future industrial approach due to its exceptional crystal quality, precise controllability, large-scale wafer production capability, and low cost. Meanwhile, van der Waals epitaxy-based CVD growth also shows the great potentials in achieving precise control of non-layered 2D Cr-based chalcogenides materials, thereby creating favorable samples quality for exploring their physical properties.

In short, there are various methods to achieve the growth of 2D Cr-based chalcogenides, and all the atomic ratio structures of Cr-based chalcogenides and the corresponding space groups and synthesis methods are given in Table 1. These abundant synthetic methods facilitate the application of 2D Cr-based chalcogenides in different fields such as optoelectronic devices, magnetic measurements and photocatalysis.

3.2 Phase control of 2D Cr-based chalcogenides by chemical vapor deposition

3.2.1 Synthesis of 2D Cr-S nanoflakes based on CVD

Currently, for the Cr-X system, the synthesis of 2D nanosheets with different phases has been successfully achieved by CVD. Recently, Wu *et al.* [117] provided a comprehensive analysis of the *in-situ* transmission electron microscopy (TEM) study on the phase transformation behavior of Cr_2S_3 at various temperatures [Fig. 6(a)]. This study elucidates the intricate mechanism underlying the phase transition process in this multiphase compound from an atomic structural perspective and offers the theoretical guidance for controlling the synthesis of multiphase materials. The annular dark-field aberration-corrected scanning transmission electron microscopy

Table 1 Structures and synthesis of 2D Cr-based chalcogenides compounds.

CrX_n (X=S/Se/Te)	Structure	Space group	Synthesis	Refs.
S	CrS_2	$P6_3/mmc$, $P3\bar{m}1$	CVD	[62]
	Cr_2S_3	$R\bar{3}$, $P\bar{3}1c$	CVD	[106]
	Cr_3S_4	$P\bar{3}m1$	–	[107]
	Cr_5S_6	$P\bar{3}1c$	–	[108]
Se	CrSe	$P6_3/mmc$	CVD, MBE, CBD	[61, 97, 101]
	$CrSe_2$	$P\bar{3}m1$, $R\bar{3}m$	Solvothermal, CVD, MBE	[92, 95, 109]
	Cr_2Se_3	$R\bar{3}$, $P\bar{3}m1$	CVD, Hydrothermal	[69, 90]
	Cr_3Se_4	$P\bar{3}m1$	–	[110]
Te	CrTe	$Cmca$, $P6_3/mmc$, $R\bar{3}m$, $Fm\bar{3}m$	MBE, CVD	[111, 112]
	$CrTe_2$	$P\bar{3}m1$, $P3m1$	CVT, CVD, MBE	[87, 113, 114]
	Cr_2Te_3	$P\bar{3}1c$	MBE, CVD	[74, 100]
	Cr_3Te_4	$C2/m$	MBE, CVD	[75, 115]
	Cr_5Te_8	$P\bar{3}m1$	CVD, CVT	[25, 55]
	$CrTe_3$	$P2/m$	MBE	[116]

(ADF-STEM) and selected area electron diffraction (SAED) images of Cr_2S_3 nanosheets at 25, 400, and 600 °C are depicted in Fig. 6(a) (left). By analyzing the atomic structure of Cr-S compounds at [001], [110], and [010] zone axis, it can be observed that a phase transition occurs at this temperature. Specifically, R-Cr_2S_3 transforms to T-Cr_2S_3, then to M-Cr_3S_4, and finally to the coexistence of M-Cr_3S_4 and T-Cr_5S_6. In addition, Fig. 6(a) (right) presents a schematic diagram illustrating the movement of the Cr atoms during the phase transition in the Cr-S compounds. The diagram reveals that the migration of Cr atoms in the CrS_2 layer to the Cr-poor layer is primarily responsible for this transition, while the horizontal movement and rearrangement of these atoms result in formation of a new phase. He *et al.* [53] explored the epitaxial growth of Cr_2S_3 nanosheets on mica substrates by atmospheric pressure CVD (APCVD) at 750 °C, showing with lateral size up to 200 μm and the single unit cell thicknesses of 1.78 nm. Moreover, the size of the samples exhibited a significant increase with growth temperature from 680 °C to 750 °C and an extension of growth time from 5 °C to 60 min. Yuan *et al.* [118] achieved *in situ* nitrogen doping of Cr_2S_3 nanosheets, inducing a transition from the $R\bar{3}$ phase to the $P\bar{3}1c$ phase and obtaining N-Cr_2S_3 nanosheets. The structures of Cr_2S_3 nanosheets before and after N doping are $R\bar{3}$ rhombohedral (P-Cr_2S_3) and $P\bar{3}1c$ trigonal (N-Cr_2S_3), respectively. 2D pure phase Cr_2S_3 (P-Cr_2S_3) and N-Cr_2S_3 were grown via a molten salt-assisted plasma-enhanced chemical vapor deposition (PECVD) method under N_2 atmosphere at 760 °C, with the SiO_2/Si substrate and quartz boat maintained at a 45° angle as shown in Fig. 6(b). The doping level of N element in N-Cr_2S_3 was adjusted by the input power of the plasma reactor. Figure 6(b) (bottom right) displays the hexagonal-shaped P-Cr_2S_3 and N-Cr_2S_3 nanosheets grown on SiO_2/Si substrate, with thicknesses of 1.79 and 1.68 nm, respectively, and lateral dimensions of approximately 10 μm. Liu *et al.* [64] used space-confined CVD with the assistance of molten salt to synthesize 1T-CrS_2 nanosheets on SiO_2/Si substrates at the temperatures of 670–680 °C. The resulting nanosheets have a semi-hexagonal morphology and possess a thickness as low as 2 nm.

3.2.2 Synthesis of 2D Cr-Se nanoflakes based on CVD

Similarly, He *et al.* [61] successfully used APCVD to epitaxially grow CrSe nanosheets on mica substrates, all of which were trigonal shapes with lateral dimensions up to 150 μm and thicknesses down to 2.5 nm. By controlling the growth temperature and source-substrate distance, high quality and large size CrSe nanosheets could be prepared, and further control of growth parameters could lead to continuous CrSe films. While the $CrSe_2$ nanosheets with controlled thickness can be successfully prepared by CVD using an epitaxial growth substrate of WSe_2 with a dangling bond-free surface [109]. Compared with SiO_2/Si substrate, it is easier to grow regular trigonal shapes with relatively lower thickness on the WSe_2 substrate. In particular, the thickness of $CrSe_2$ strongly depends on the growth temperature. The average thickness increases from 4 to 7 nm as the temperature raises from 700 °C to 710 °C, and further reaches 10 nm when the temperature is elevated to 720 °C. Moreover, Wang *et al.* [70] explored the thermodynamic effects on the growth of 2D Cr_2Se_3 nanosheets and successfully synthesized rhombohedral Cr_2Se_3 nanosheets with adjustable thickness by CVD on various substrates such as mica, SiO_2/Si, and glassy silica. As shown in Fig. 6(c), the XRD pattern indicates that the Cr_2Se_3 nanosheets grown on SiO_2/Si substrate exhibit the (001) orientation, excellent single crystallinity, and high crystal quality. As can be observed from the optical images in Fig. 6(c) (bottom),

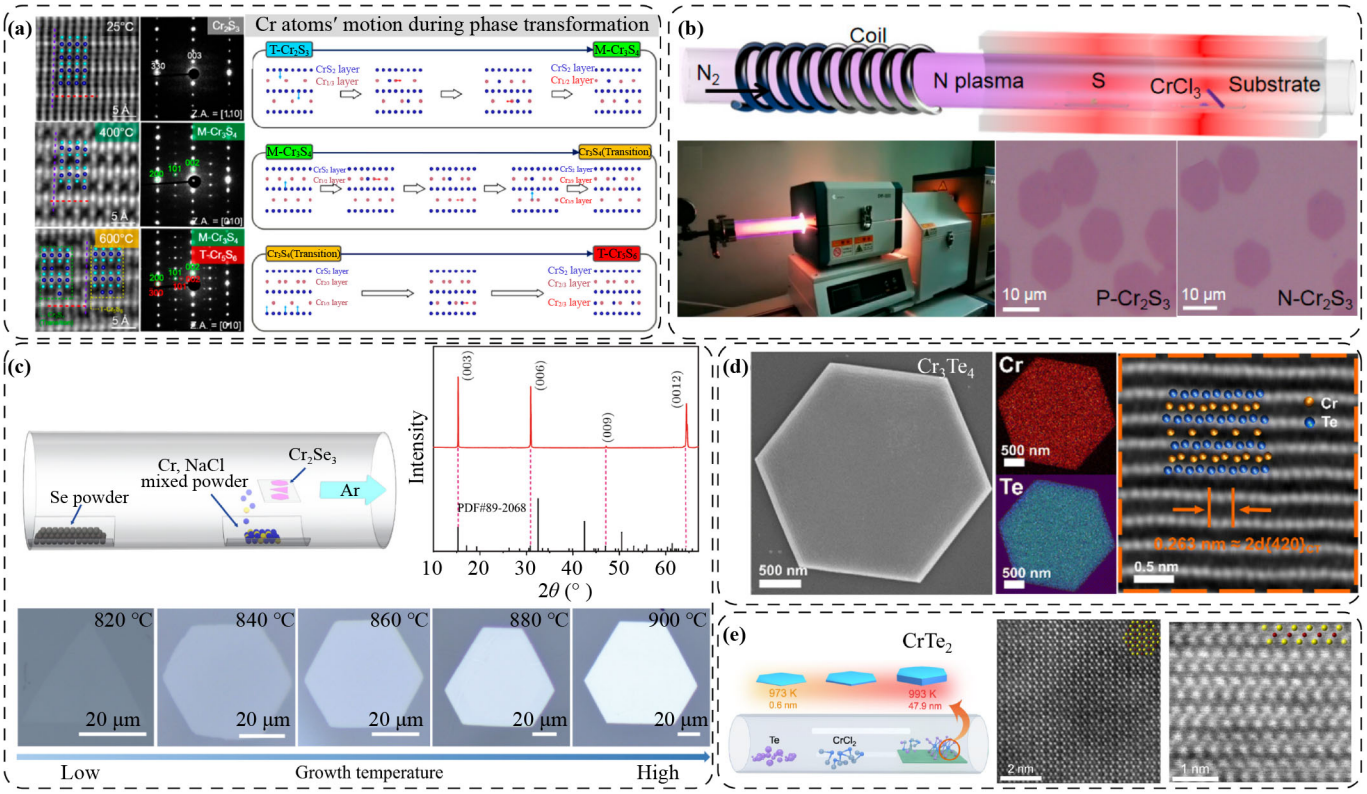

Fig. 6 Schematic illustration and characterization of the synthesis of 2D Cr-based chalcogenides in different phases based on chemical vapor deposition. **(a)** ADF-STEM and SAED images of Cr_2S_3 at 25, 400, and 600 °C, respectively (left); schematic representation of the atomic movement process of Cr in Cr_2S_3 during the phase transition (right) [117]. **(b)** PECVD synthetic process for N-doping in Cr_2S_3 nanosheets, and the OM images of P-Cr_2S_3 and N-Cr_2S_3 synthesized on SiO_2/Si substrates [118]. **(c)** Schematic illustration of CVD synthesis of Cr_2Se_3 (top left) and XRD spectra of two-dimensional Cr_2Se_3 nanosheets (top right); OM images of the synthesized Cr_2Se_3 nanosheets at different temperatures (bottom) [70]. **(d)** SEM image of Cr_3Te_4 nanoflakes and corresponding EDS mapping images with Cr and Te (left); the cross-sectional ADF-STEM image of Cr_3Te_4 nanoflakes and corresponding atomic structures (right) [119]. **(e)** A CVD synthesis route of 1T-$CrTe_2$ and atomic-resolution STEM-HADDF images of top-view and cross-section [113].

the thickness of Cr_2Se_3 nanosheets on mica substrates increases from 1.8 nm to tens of nm as the growth temperature from 820 to 900 °C, and the lateral size can increase to 120 μm with the changed shapes from triangular to hexagonal. In contrast, the optical microscope (OM) of Cr_2Se_3 on SiO_2/Si and glass substrates are predominantly triangular nanosheets. This phenomenon may be attributed to the factor of the different nucleation potential of Cr_2Se_3 on different substrate surfaces.

3.2.3 Synthesis of 2D Cr-Te nanoflakes based on CVD

In the Cr-Te system, addressing the issue of structural diversity is crucial during material growth, and CVD method serves as a vital tool for achieving phase modulation. Duan *et al.* [75] employed the APCVD method to synthesize Cr_3Te_4 nanosheets on SiO_2/Si substrates, adding 15 sccm H_2 to the transport carrier gas Ar in order to achieve an adequate supply of Te. Similarly, the nanosheets exhibited a precise temperature-dependent thickness variation down to 1 nm at 670 °C. Recently, Zou *et al.* [119] achieved epitaxial growth of Cr_3Te_4 nanosheets on mica substrates with a thickness ranging from 10 to 150 nm, as illustrated in Fig. 6(d). The scanning electron microscope (SEM) image reveals a typical hexagonal nanosheet with an exceptionally smooth surface and a highly uniform distribution of Cr and Te elements. A cross-sectional STEM analysis of this sample, as depicted in Fig. 6(d) (right), presents a clear the atomic arrangement that is consistent with the Cr_3Te_4 structure. Gong *et al.* synthesized 2D 1T-$CrTe_2$ nanosheets of controlled thickness on SiO_2/Si substrates using $CrCl_2$ and Te precursors by CVD, as shown in Fig. 6(e) [113]. The effect of reaction temperature ranging from 973 to 993 K on the synthesis of samples was investigated in details. As a result, the thickness of single crystalline 1T-$CrTe_2$ nanosheets gradually increased from 1.2 nm to about 50 nm as the growth temperature increased, while all nanosheets showed hexagonal structures. Further STEM analysis was conducted on 1T-$CrTe_2$, revealing an atomic-resolved STEM-HAADF image from a top view that clearly

depicts the well-organized arrangement of atoms in a hexatomic ring. This observation, as shown in Fig. 6(e) (middle), reflects the six-fold symmetry of 1T-$CrTe_2$, which corresponds to its hexagonal morphology. The cross-sectional STEM in Fig. 6(e) (right) shows that the atomic arrangement is consistent with the atomic structure of 1T-$CrTe_2$, providing the evidence for successful preparation of layered 1T-$CrTe_2$ nanosheets. In addition, Zhou *et al.* [55] achieved the preparation of Cr_5Te_8 nanosheets using pure Ar with a larger flow rate (200 sccm) as the carrier gas. Furthermore, Liu *et al.* [60] provided a method for synthesizing very large size CrTe nanosheets. Using a mixture of Cr and $CrCl_3{\cdot}6H_2O$ as the metal precursor source and Te powder as the Te precursor, 5 nm single crystal of CrTe nanosheets with lateral dimensions up to 250 μm were synthesized on SiO_2/Si substrates at 700 °C. The control of the reaction rate is primarily achieved by regulating the ratio of Cr and $CrCl_3{\cdot}6H_2O$ in the mixed Cr precursor, while Te is added to reduce the melting point of the Cr metal. Using this method, the growth of 250 μm nanosheets can be accomplished within a mere 2 min, which greatly improves the sample preparation efficiency. The above synthesis for Cr-Te compounds involves modifying the precursor type, carrier gas and growth temperature to achieve the phase structure modulation of Cr_xTe_y. However, the thickness and size of the nanosheets are strongly influenced by the growth temperature and time. In conclusion, the phase control of Cr-based chalcogenides based on CVD growth method is a feasible and high-quality approach for preparing single crystals with special phases, which can be applied in 2D optoelectronic and magnetoelectronic devices.

4 Properties and applications of 2D CrX_n nanoflakes

4.1 Two-dimensional Cr-based heterojunctions

In recent years, the family of 2D Cr-based chalcogenides has been continuously expanded, and 2D heterojunctions based on CrX_n (X = S, Se and Te) have likewise received widespread attention. Zheng *et al.* [120] used first principle calculations to understand the electronic and optical properties of InSe/CrS_2 heterojunction. Figure 7(a) (left) illustrates the positions of the band edges of CrS_2 and InSe, respectively, which are relative to the vacuum energy level. It is evident that electron-hole transfer occurs from InSe to CrS_2 across the interface of their heterojunction. Further calculation of the energy bands and density of states of the InSe/CrS_2 vdWH, as shown in Fig. 7(a) (right), indicates that the conduction band of this heterojunction is mainly contributed by the CrS_2 layer. However, the valence band is contributed by both CrS_2 and InSe. The monolayer CrS_2 and InSe undergo the coupling of the valence band, which is somewhat different from Fig. 7(a) (left). This van der Waals heterojunction exhibits an intrinsic mixed band alignment with a band gap of 1.2 eV. PDOS calculations reveal that by manipulating the electric field, a finely tuned mixed-band alignment can be achieved between type-I and type-II. Consequently, this heterojunction holds significant potential for applications in optical and optoelectronic devices. Cao *et al.* [121] conducted a theoretical investigation on the electronic structure of the CrS_2/BP heterojunction, as depicted in Fig. 7(b). The energy band dispersion of the heterojunction indicates that both the CBM and VBM are located at the K point, resulting in an extremely narrow direct band gap with a value of E_g = 0.221 eV. From the P-DOS calculations, the VBM and CBM of the CrS_2/BP heterojunction are mainly attributed to the P-p and Cr-d orbitals, respectively. These properties endow the heterojunction with a broader optical absorption and a more favorable energy band structure for carrier transport. The nonequivalent energy valleys present in the first Brillouin zone of TMD materials render them a promising candidate for valley electronics. Therefore, Xiong *et al.* [122] investigated the effect of axial strain on the valley splitting of WSe_2 based on the WSe_2/$CrSe_2$ heterojunction. As shown in Fig. 7(c), the red bubbles represent the contribution of the W element, and the spin splitting between K(α) and K'(α') varies under different strains, thereby resulting in magnetically induced valley splitting. A notable feature is that the bottom of energy valley shifts away from the high symmetry point under uniaxial strain, which can be attributed to the reduced crystal symmetry of TMDs. When the uniaxial strain is increased, the reduction of the structural symmetry leads to the decrease or even disappearance of the valley splitting phenomenon, which has significant implications for the field of valley electronics.

Duan *et al.* [109] synthesized a $CrSe_2$/WSe_2 heterojunction, as shown in Fig. 7(d) (left). The distribution of individual elements in the low-resolution TEM-EDS mapping clearly reveals that typical trigonal $CrSe_2$ nanosheets grow on the surface of the WSe_2 film. Figure 7(d) (right) demonstrates that the heterojunction possesses two sets of six-fold-symmetric diffraction spots in the SAED image, which show the lattice spacings of 0.289 and 0.314 nm, corresponding to the (100) plane of WSe_2 and $CrSe_2$, respectively. Additionally, its high-resolution TEM images also reveal the well-defined moiré superlattice. The ferromagnetic properties of the heterojunction were further investigated. It was found that there were obvious thickness-dependent ferromagnetic properties of the $CrSe_2$ nanosheets, which were primarily attributed to the charge transfer of WSe_2 and the interlayer coupling within $CrSe_2$. Samarth *et al.* [123] synthesized monolayer 1T-$CrTe_2$ and $ZrTe_2$/$CrTe_2$ heterojunction on a (001) sapphire substrate using MBE, and the cross-sectional HAADF-STEM view of this heterojunction is shown in Fig. 7(e) (left). In addition, a single layer of

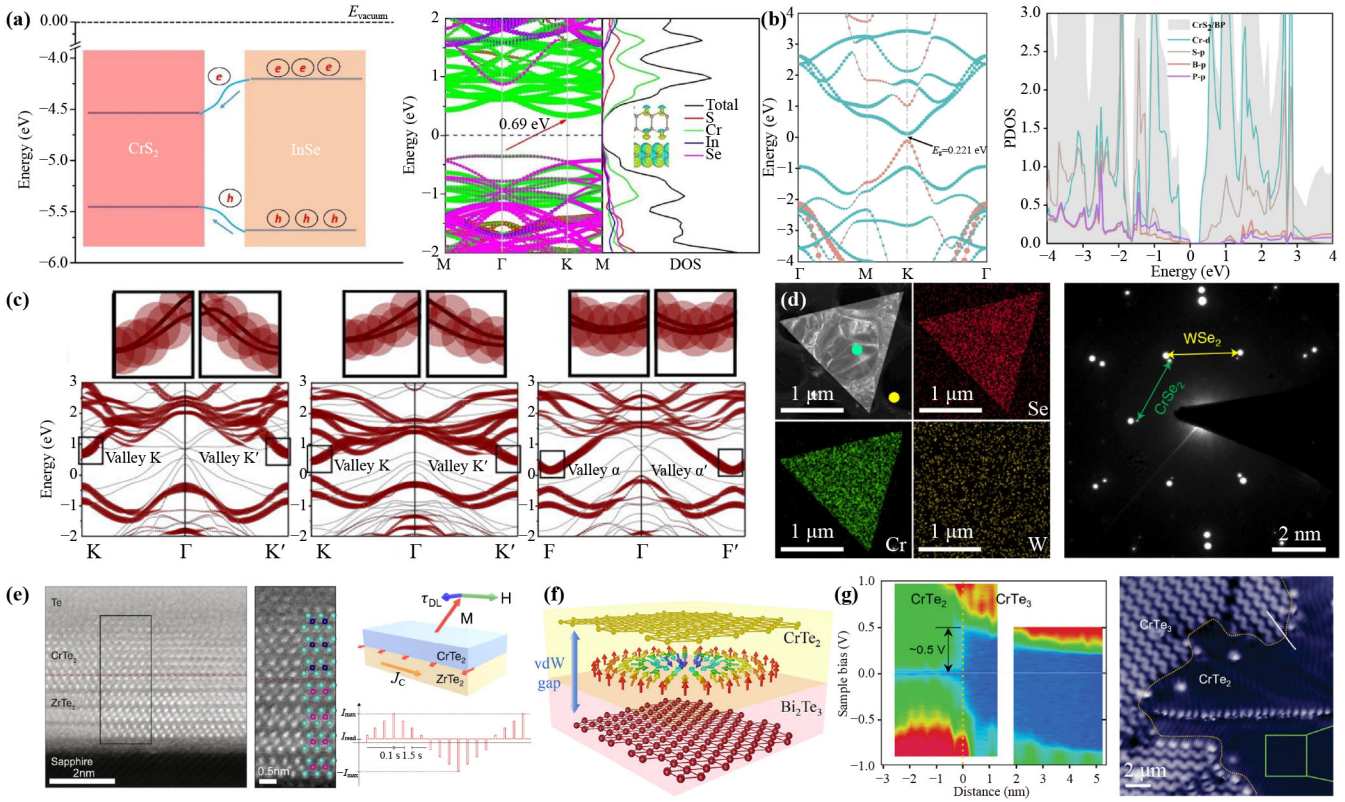

Fig. 7 Heterojunction properties of 2D Cr-based sulfides. **(a)** Energy band distribution of the relative vacuum energy levels of monolayer CrS_2 and InSe and DFT calculation of the electronic energy band structure and density of states of CrS_2/InSe heterojunction [120]. **(b)** Energy band structure and PDOS of CrS_2/BP heterojunction, where blue and pink lines are CrS_2 and BP, respectively [121]. **(c)** Projected energy band structures of W atoms in $WSe_2/CrSe_2$ heterojunctions with no strain, 10% biaxial strain and 10% uniaxial strain [122]. **(d)** Low-resolution TEM image of the $CrSe_2/WSe_2$ heterojunction and EDS elemental mapping of Cr, Se, and W, and the SAED pattern of this heterojunction [109]. **(e)** Cross-sectional HADDF-STEM images of $ZrTe_2/CrTe_2$ heterojunction and SOT-assisted magnetization switching schematic of $ZrTe_2/CrTe_2$ heterojunction device [123]. **(f)** Schematic diagram of the $CrTe_2/Bi_2Te_3$ bilayer heterojunction structure with a van der Waals gap [124]. **(g)** The dI/dV conductance mapping at the $CrTe_2/CrTe_3$ metal-semiconductor lateral heterojunction interface and the STM image of this monolayer lateral heterojunction [125].

1T-$CrTe_2$ grown on the $ZrTe_2$ surface was found to still have long-range ferromagnetic ordering. The $CrTe_2$/$ZrTe_2$ heterojunction Hall bar device was constructed, as shown in Fig. 7(e) (right). And the relationship between the magnetization to the current for the $CrTe_2$ was probed by anomalous Hall effect (AHE), which proved that the current flows in parallel in both $ZrTe_2$ and $CrTe_2$ layers. Herein, the current-induced magnetization switching of this ferromagnetic $CrTe_2/ZrTe_2$ heterojunction device was realized. The successful fabrication of wafer-scale vdW 2D ferromagnets and topological semimetallic heterojunctions can catalyze the exploration of integrated quantum devices for advanced research. Bian *et al.* [124] employed molecular beam epitaxy to create a 2D vdW ferromagnet/topological insulator heterojunction consisting of $CrTe_2/Bi_2Te_3$ with several atomic layer thicknesses, separated by a van der Waals gap as depicted in Fig. 7(f). In this heterojunction, a significant topological Hall effect (THE) signal is observed with a resistivity of up to 1.39 μΩ·cm at 10 K (much larger than that of bilayer heterojunctions [126–128]), which is mainly due to the combination of the 2D ferromagnetism of $CrTe_2$, the strong spin-orbit coupling of Bi_2Te_3, and the atomic-level sharp interface. Zhao *et al.* [125] synthesized monolayer and bilayer antiferromagnetic $CrTe_3$ on HOPG with semiconducting properties, exhibiting band gaps of 0.92 eV and 0.71 eV, respectively. By annealing the monolayer of $CrTe_3$, a portion of the monolayer can transform into a monolayer $CrTe_2$, resulting in the formation of lateral magnetic metal-semiconductor heterojunctions ($CrTe_2/CrTe_3$) with strong chemical bonding at the interface. In Fig. 7(g) (right), this in-plane heterojunction clearly observed by the atomic resolution STM images. Additionally, the dI/dV conductivity map presented in Fig. 7(g) (left) clearly illustrates the energy band bending state at the heterojunction interface, which is a typical characteristic of Schottky barriers observed at metal-semiconductor interface. The height of the Schottky barriers were measured to be approximately 0.5 V. Simultaneously, they predicted

that the antiferromagnetic and ferromagnetic behaviors of this heterojunction or the metal and semiconductor properties of this heterojunction could switch over time under the in-plane stresses. Moreover, Lin *et al.* [51] also prepared a Cr_2Te_3/Cr_5Te_{8tr} lateral heterojunction. Unlike the $CrTe_2/CrTe_3$ heterojunction, this one has a mixed-phase transition region of about 1 μm between Cr_2Te_3 and Cr_5Te_{8tr}, in which the state of the Cr_xTe_y phase is random and the arrangement of Cr atoms is disordered. This transition region has a great influence on the magnetic decoupling effect of the Cr_2Te_3/Cr_5Te_{8tr} lateral heterojunction, enabling the maintenance of magnetism up to 210 K. Based on the above theoretical and experimental study, we can see that Cr-based chalcogenides heterojunction devices exhibit rich electrical and magnetic properties, which can play an important role in the future applications of magnetism and spintronics.

4.2 Magnetic properties of two-dimensional Cr-based materials

Since the experimental demonstration of 2D magnetism, extensive research has been conducted in the field of 2D magnetic materials. Meanwhile, the emergence of 2D transition metal chalcogenides, particularly Cr-based chalcogenides, which exhibit excellent ferromagnetism, anomalous Hall effect and magnetic anisotropy, has also garnered significant attention from researchers. These properties are key to future applications in spintronic and magnetoelectronic, and magneto-optoelectronic devices.

4.2.1 Ferromagnetic properties of 2D CrX_n materials

Cr-based halides, such as CrI_3 and $CrBr_3$, exhibit ferromagnetic behavior in the monolayer limit with a pronounced layer dependence [31, 129]. Extensive studies have also been conducted on the ferromagnetism of other Cr-based chalcogenides, especially Cr-S, Cr-Se and Cr-Te compounds [67, 72, 79, 130]. Notably, some of these compounds demonstrate Curie temperatures (T_C) above room temperature including but not limited to Cr_2Te_3, Cr_3Te_4, and CrSe [61, 74, 115]. The magnetic phase diagram of $CrSe_2$, as shown in Fig. 8(a) (left), indicates that the T_C remains at 110 K until the number of layers is reduced to 16 [109]. However, as the number of layers decreases, there is a significant reduction in the Curie temperature and ultimately, for a single layer, it drops to 65 K. A Hall bar device of 7-layer $CrSe_2$ was constructed to investigate its magnetic transport properties. The anomalous Hall effect is shown in Fig. 8(a) (right), and both the residual anomalous Hall resistance and coercivity exhibit a decreasing trend with increasing temperature. Furthermore, the magnetic transport properties confirm that the CVD-synthesized $CrSe_2$ nanosheets possess typical ferromagnetic characteristics. Wang *et al.* [107] utilized first-principles calculations to predict a series of Cr_3X_4 monolayers, among which Cr_3S_4 exhibits ferrimagnetism while both Cr_3Se_4 and Cr_3Te_4 display ferromagnetism. The Heisenberg model suggests that strong ferromagnetic ordering is enabled by significant inter- and intra-layer coupled exchange interactions in the monolayers of Cr_3Se_4 and Cr_3Te_4. The Monte Carlo method was employed to simulate the temperature-dependent magnetization and specific heat capacity of monolayer Cr_3Se_4 and Cr_3Te_4, as depicted in Fig. 8(b). It was discovered that the T_C of monolayer Cr_3Se_4 and Cr_3Te_4 are 370 and 460 K, respectively, which surpass those of other 2D van der Waals materials. These findings suggest that monolayer Cr_3Se_4 and Cr_3Te_4 hold great potential as prime candidates for spintronic devices.

Xu *et al.* [91] conducted superconducting quantum interference device (SQUID) measurements to investigate the room temperature ferromagnetism of $CrTe_2$ thin films, as illustrated in Fig. 8(c). The magnetization of the $CrTe_2$ films decreases significantly with increasing temperature under field cooling and a perpendicular external magnetic field of 1000 Oe. Even when reduced to three layers, the $CrTe_2$ film maintains a T_C near room temperature, and at seven layers, it exhibits a significant magnetization at 300 K, indicating its maintained ferromagnetic ordering at this temperature. Figure 8(c) (right) gives the out-of-plane hysteresis of the seven-layer $CrTe_2$ film at different temperatures, with its coercive field increasing to 1000 Oe as the temperature drops from 300 to 20 K, indicating typical hard magnet behavior. Furthermore, through X-ray magnetic circular dichroism (XMCD) characterization, it has been demonstrated that even a single layer of $CrTe_2$ can still exhibit high Curie temperatures ($T_C \sim 200$ K). Later, they explored the intercalation of Cr atoms to achieve antiferromagnetic interlayer exchange coupling in Cr_5Te_8, presenting a novel approach for designing two-dimensional magnetic structures [25]. Previous research has established that Cr_5Te_8 is comprised of van der Waals $CrTe_2$ materials with interlayer Cr atoms, in which the $CrTe_2$ interlayers exhibit robust ferromagnetism. However, the insertion of interlayer Cr atoms greatly affects the magnetic transport of Cr_5Te_8, resulting in an antiparallel spin configuration. The T_C of Cr_5Te_8 is determined to be approximately 150 K based on the variation curves of magnetization intensity with temperature under different magnetic fields. With the increase of temperature, this Cr_5Te_8 sample exhibits typical antiferromagnetic behavior with a Néel temperature (T_N) of 180 K. As the magnetic field increases, the T_N decreases until it disappears when the magnetic field exceeds 0.5 T. A schematic diagram depicting the electrical transport device of Cr_5Te_8 is presented in Fig. 8(d) (left). As the temperature approaches T_C, a sharp peak emerges in the resistance of the device, and with further increase in temperature, the peak broadens significantly, signifying a magnetic phase transition from ferromagnetic to anti-

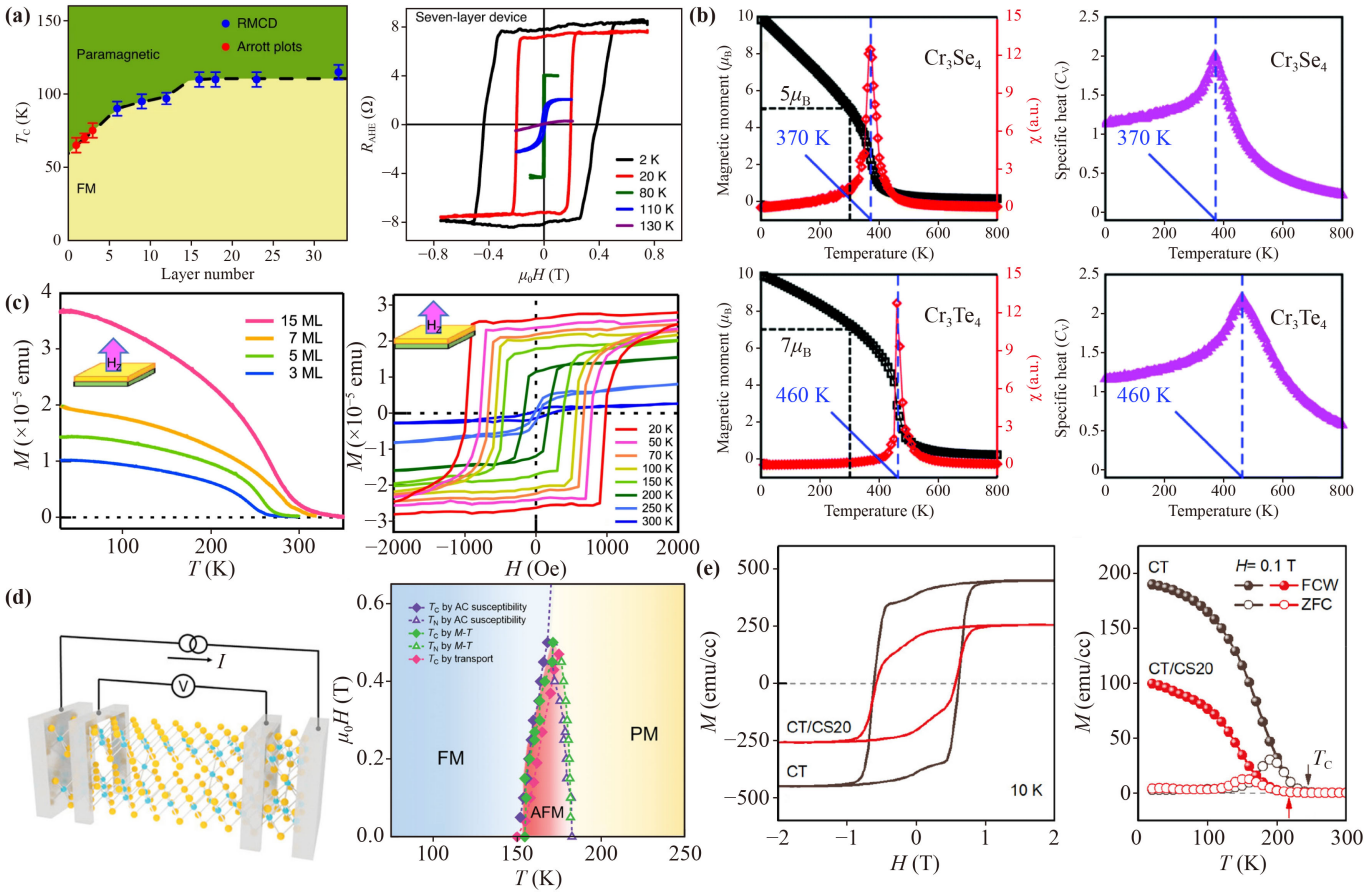

Fig. 8 Magnetic properties of Cr-based sulfides. **(a)** Layer-dependent properties of the Curie temperature (T_C) of $CrSe_2$ and anomalous Hall resistance (R_{AHE}) variation of seven layers of $CrSe_2$ at given temperatures [109]. **(b)** Magnetic moments (μ_B), magnetization (χ) and specific heat (C_V) of monolayers of Cr_3Se_4 and Cr_3Te_4 as a function of temperature, simulated using the Monte Carlo method based on the 2D Heisenberg model [107]. **(c)** Magnetic temperature curves of $CrTe_2$ films with different thicknesses in field-cooling mode (left) and vertical magnetization curves of 7 ML $CrTe_2$ sample at different temperatures (right) [91]. **(d)** Schematic diagram of electrical transport measurements of Cr_5Te_8 devices under magnetic field and magnetic field-temperature phase diagram of Cr_5Te_8 [25]. **(e)** Hysteresis curves of Cr_2Te_3 and Cr_2Te_3/Cr_2Se_3 heterojunctions at 10 K and their temperature dependent magnetization intensity after field cooling and zero field cooling [131].

ferromagnetic phase. The magnetic phase transition diagram of Cr_5Te_8 is presented in Fig. 8(d) (right), where the joint modulation of temperature and magnetic field enables the realization of ferromagnetic, antiferromagnetic, and paramagnetic phase transitions in Cr_5Te_8. Chun *et al.* [131] investigated the THE resulting from interlayer exchange coupling in ferromagnetic Cr_2Te_3/noncoplanar antiferromagnetic Cr_2Se_3 (CT/CS) heterojunctions. Firstly, the magnetization curves of CT and CT/CS are compared in Fig. 8(e). The fabricated heterojunction significantly reduces the saturated magnetization of CT but does not substantially alter the magnitude of the coercive field and causes a slight decrease for the magnetic phase transition temperature. The presence of noncoplanar ordering in the antiferromagnet plays a crucial role in the generation of the topological Hall effect. Measurement of the topological Hall resistivity of CT/CS heterojunctions with different Cr_2Se_3 thicknesses indicates that the THE intensity remains unaffected by sample thickness, and disappears beyond the Néel temperature. This topological Hall effect observed in CT/CS heterojunctions arises from the interfaces between the ferromagnetic (FM)/noncoplanar antiferromagnetic (AFM) materials with antisymmetric exchange coupling, providing a promising avenue for investigating the interplay between interfacial exchange and spin chirality.

In ferromagnetic materials, the Curie temperature normally decreases significantly as the material size is reduced, such as CrTe and Cr_5Te_8 [94, 112]. However, He *et al.* [74] investigated the ferromagnetism of 2D Cr_2Te_3 and observed an opposite trend: when the thickness of Cr_2Te_3 nanosheets was decreased from 40.3 to 7.1 nm, the T_C increased from 160 K to 280 K due to atomic reconfiguration in low dimensions. In addition, Zhang *et al.* [44] obtained symmetry-broken layered $Cr_{1.5}Te_2$ nanosheets by precisely modulating the Cr atom intercalation and investigated the ferromagnetic behavior for

self-intercalated $Cr_{1+x}Te_2$ nanosheets using MOKE measurements. The Curie temperature observed in $Cr_{1.5}Te_2$ nanosheets was (285 ± 5) K, which is similar with that of bulk materials and does not vary with thickness. This interesting variation of Curie temperature due to Cr atom intercalation is a unique property of Cr-based chalcogenides, which help obtain ferromagnetic 2D materials with high Curie temperature [132, 133]. In conclusion, the abundant ferromagnetism exhibited by 2D Cr-based chalcogenides positions them as a crucial member of the 2D magnetic material family. The construction of 2D Cr-based chalcogenides heterojunctions and the alteration of Cr atom intercalation can provide more possibilities for their applications in spintronic devices.

4.2.2 Magnetic modulation and magnetic anisotropy of 2D CrX_n chalcogenides

The magnetic properties of Cr-based chalcogenides are of great significant importance in spintronics, and the high Curie temperature of 2D magnetic materials has been a focal point in research on magnetic materials. As previously mentioned, Cr-based chalcogenides can exhibit high ferromagnetic phase transition temperature by adjusting the concentration of Cr intercalation layer. Furthermore, in 2D materials, the ferromagnetic properties such as Curie temperature and coercive field can be easily manipulated through external adjustments, which can greatly enhance their magnetic characteristics and expanding their potential applications in spintronic devices. The strain-modulated reflective magnetic circular dichroism (RMCD) sweeps of Cr_2Te_3 nanosheets at different temperatures are given in Fig. 9(a) [134]. The coercive field of Cr_2Te_3 nanosheet decreases significantly (only 4% of that of the unstrained nanosheet) at tensile strain (+0.37%), while the T_C increases from 140 to 180 K. However, when a compressive strain (–0.37%) is applied, the T_C drops from 140 to 110 K and simultaneously, the coercive field also experiences a significant reduction (about 33% of that of unstrained Cr_2Te_3). Moreover, the reduction of T_C caused by the compressive strain becomes more significant with increasing thickness of the nanosheets, resulting in an enhanced negative modulation that can lower T_C to 90 K. This stress-induced alteration of magnetism is mainly attributed to the changes in super-exchange interaction between the ions due to variations in Cr–Te–Cr angle under uniaxial strain, with larger angles contributing more significantly to magnetism. The angle increases from 131.8° to 132.3° when the strain increases from –1.0% to +1.0%, which is also reflected in the increase of T_C. In addition, Moodera *et al.* [135] have investigated the impact of strain in the magnetic modulation of Cr_2Te_3. It was discovered that AHE exhibits a unique sign reversal with a hump-shaped Hall feature under the varying temperature and strain, which is mainly related to the presence of multiple magnetic layers/domains under interface strain conditions. Duan *et al.* [136] conducted a comprehensive analysis using DFT calculations to investigate the impact of strain and Cr atom intercalation on the magnetic properties of $CrTe_2$. The transition of $CrTe_2$ from intra-layer antiferromagnetic coupling to ferromagnetic coupling, and ultimately to inter-layer antiferromagnetic coupling, occurs as the applied strain changes from –6% to 4%. This phenomenon is attributed to the alteration in super-exchange interaction resulting from increased distances between the Cr atoms in the facets and decreased inter-layer spacing. In the meantime, the Cr intercalation within the $CrTe_2$ layers induces a transition of $CrTe_2$ to ferromagnetism. These tunable magnetic transitions hold great significance for further exploration of $CrTe_2$-based magnetic strain sensors and spin transistors.

The tunable magnetic properties of such 2D materials effectively expand their investigation fields in magnetism and spintronics. Furthermore, the complex magnetic properties of Cr-based sulfides that are yet to be discovered are gradually being explored. Banerjee *et al.* [100] were the first to discover the possible spin-glass behavior in MBE-grown Cr_2Te_3, where a spin-glass phase emerged in Cr_2Te_3 nanosheet below 35 K, resulting in the randomization of magnetic moments and a rapid decline in magnetization strength. Later, Zhou *et al.* [137] reported the observation of intriguing spin-glass states in two-dimensional Cr_2Se_3 nanosheets with a spin-freezing temperature of 28 K. Notably, an increase in frequency led to a significant enhancement in the spin-freezing temperature of Cr_2Se_3 nanosheets, as depicted in Fig. 9(b). The inherent spin glass behavior in 2D Cr-based materials arises from the geometrical frustration of their crystalline symmetry, providing a foundation for investigating the disordered spin in 2D systems.

Anisotropic magnetoresistance (AMR) is an inherent property exhibited by ferromagnetic materials. Since the discovery of the ferromagnetism of 2D Cr-based materials, their magnetic anisotropy has been successively reported. Banerjee *et al.* [100] conducted magneto-transport measurements on a 4 nm Cr_2Te_3 nanosheet, which displayed typical metallic material-like AMR, as illustrated in Fig. 9(c). The magnetic resistance (MR) of a 4 nm Cr_2Te_3 nanosheet varies with the direction of the magnetic field, indicating the presence of perpendicular magnetic anisotropy (PMA) in the film. Additionally, Zheng *et al.* [139] observed a semiconducting-to-metallic transition at 175 K in MBE-grown epitaxial films of Cr_2Te_3. Negative MR effects were observed in all Cr_2Te_3 films, with the strongest effect occurring at T_C. The PMA of the films is indicated by their AHE and out-of-plane hysteresis, with the susceptibility magnetization axis along the *c*-axis direction. Furthermore, the magnetic transport measurements for different magnetic field directions show that Cr_2Te_3 has a typical

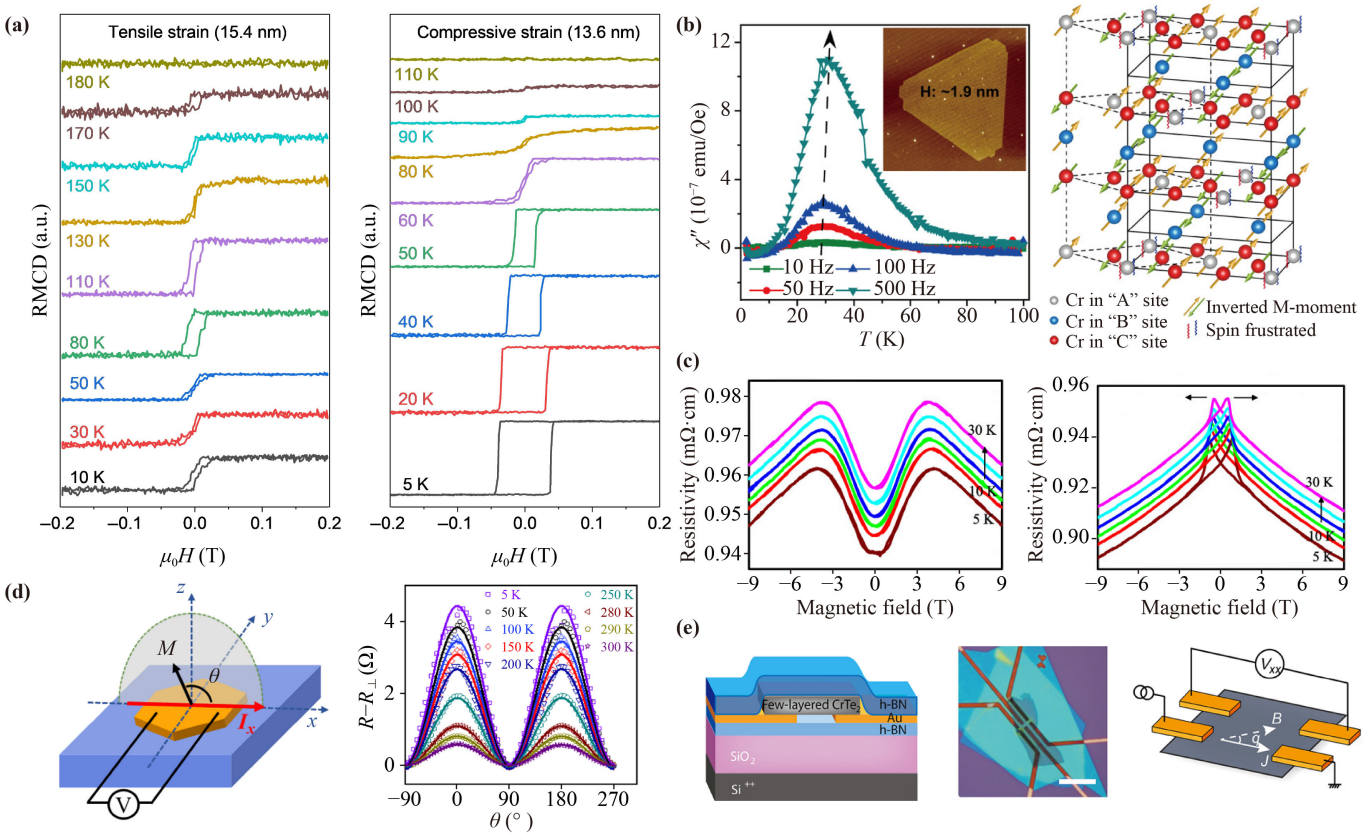

Fig. 9 Novel magnetic properties of 2D Cr-based materials. **(a)** RMCD sweeps of Cr_2Te_3 nanosheets under +0.37% tensile strain (15.4 nm) and –0.37%compressive strain (13.6 nm) at different temperatures [134]. **(b)** Temperature-dependent characteristics of the out-of-plane phase of magnetization at different frequencies (f = 10, 50, 100 and 500 Hz) [137]. **(c)** Magnetoresistance (MR) properties of Cr_2Te_3 at parallel (θ = 90°) and perpendicular (θ = 0°) magnetic fields and variation of MR with magnetic field direction at 2 K [100]. **(d)** Illustration of the measured magnetoresistance of CrTe under an out-of-plane magnetic field and the temperature-dependent characteristics of the resistance at different θ under a 4 T magnetic field [138]. **(e)** Schematic and optical diagrams of a few-layer $CrTe_2$ device, and schematic diagrams of anisotropic magnetoresistance measurements [87].

anisotropic magnetoresistance, in which the out-of-plane magnetoresistance is significantly larger than that of in-plane magnetoresistance. The AMR of ferromagnetic CrTe nanosheets was investigated by Zhai *et al.* [138], and the device schematic along with the AMR results are depicted in Fig. 9(d). These hexagonal CrTe nanosheets exhibit the magnetization along their normal direction, and the AMR ratio exhibits a linear increase as the room temperature decreases, reaching 5.2% at 5 K, which is comparable to that of numerous magnetic metals and alloys. To investigate the spin transport properties of 1T-$CrTe_2$, Zhang *et al.* [87] fabricated h-BN/$CrTe_2$/h-BN devices on SiO_2/Si substrates, as illustrated in Fig. 9(e). Remarkably, $CrTe_2$ exhibits a negative/positive AMR at ambient/low temperature, demonstrating an entirely contrasting AMR behavior compared to other vdW 2D ferromagnetic materials. Zhang *et al.* [80] analyzed the THE of $Cr_{1.2}Te_2$ and observed a significant magnetic field angle dependence of the Hall resistivity in the nanosheets, while the magnetic field angle dependence measurements of the magnetoresistance also proved the existence of AMR.

In summary, the 2D Cr-based chalcogenide materials exhibit exceptional physical properties, such as high Curie temperature, tunable ferromagnetism, anomalous Hall effect and anisotropic magnetoresistance, render them highly promising candidates for magnetic storage and spintronic devices. Besides, it is crucial to explore additional avenues for optimizing the ferromagnetic properties of 2D Cr-based chalcogenides materials and uncovering novel physical phenomena in order to enhance the application fields for these 2D CrX_n compounds.

4.3 Novel optoelectronic properties of 2D CrX_n materials

4.3.1 Nonlinear optical characteristics of 2D CrX_n

The diverse phases of Cr-based chalcogenides have led to the development of a family of materials with great potential for various applications, such as nonlinear optics, electronic and optoelectronic devices. The

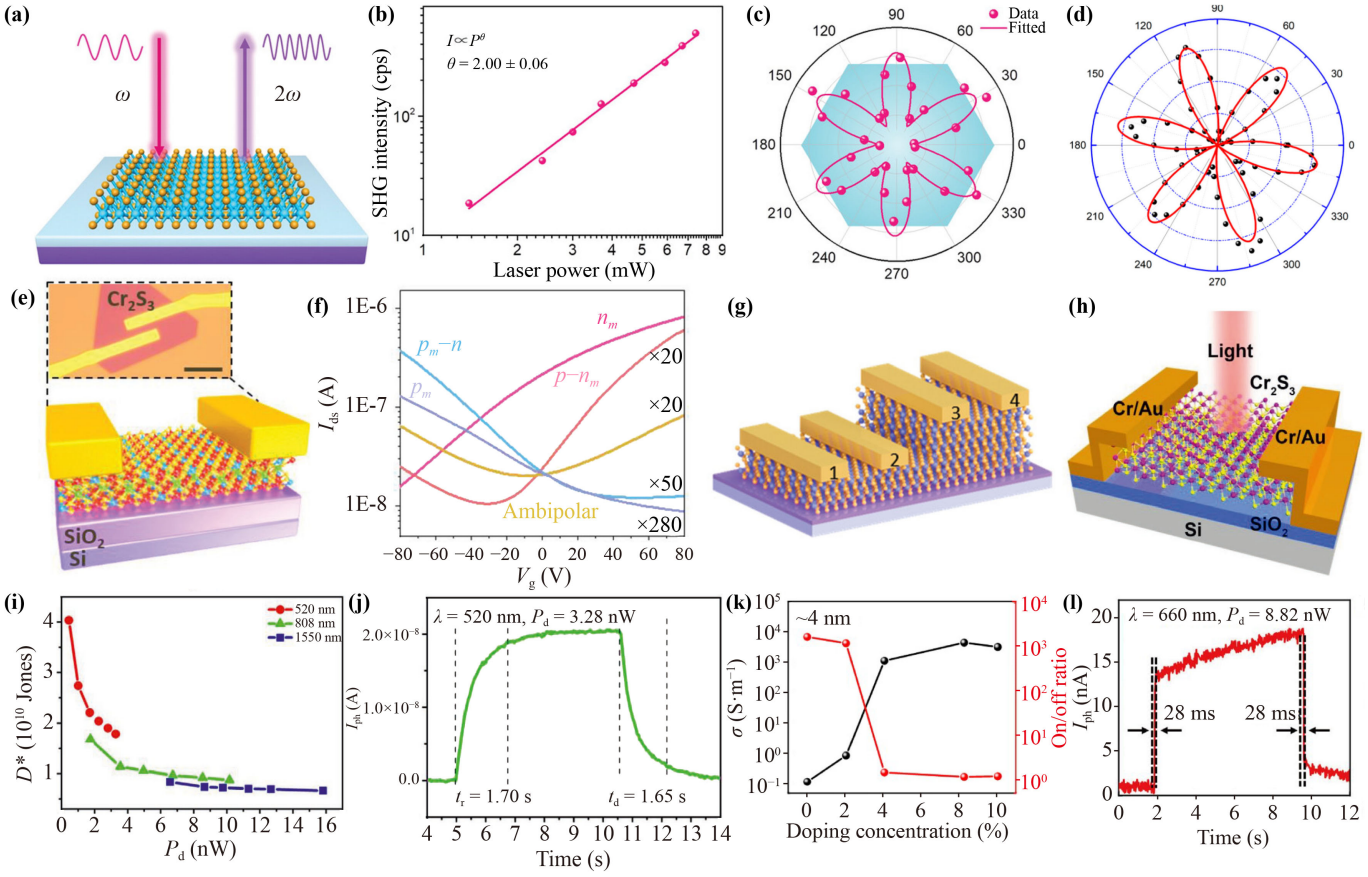

Fig. 10 **(a)** Schematic of SHG measurement of Cr_5Te_8 nanosheets. **(b)** SHG intensity dependence characteristics with laser power. **(c)** Angle polarization SHG of Cr_5Te_8 nanosheets [94]. **(d)** Angle-polarized SHG of monolayer Cr_2S_3 [53]. **(e)** Schematic diagram and OM image of Cr_2S_3 electrical device. **(f)** Transfer characteristic curves (I_{ds}–V_g) of Cr_2S_3 nanosheets with different thicknesses (V_{ds} = 1 V, thickness of Cr_2S_3 nanosheets are 2.6, 3.6, 4.8, 6 and 7.6 nm, respectively) [106]. **(g)** Schematic diagram of Cr_2S_3 homojunction transistor [105]. **(h)** Device schematic of Cr_2S_3 photodetector. **(i)** Detectivity dependence of Cr_2S_3 photodetector with effective laser power at different laser wavelengths (520, 808 and 1650 nm). **(j)** Time-resolved photocurrent of Cr_2S_3 photodetector at V_{ds} = 1 V, a 520 nm laser and 3.28 nW laser power [142]. **(k)** Conductivity (black) and on/off ratio (red) of Cr_2S_3 transistors with Se doping concentration, respectively. **(l)** Time-resolved photoresponse of a Se doped Cr_2S_3 transistor at V_{ds} = 1 V and 3.28 nW laser power [143].

schematic of second harmonic generation (SHG) is shown in Fig. 10(a), showing the process where two photons with a frequency of ω are incident on a nonlinear optical medium and interact to emit a photon with doubled-frequency of 2ω [94]. Xu *et al.* [94] investigated the nonlinear optical properties of Cr_5Te_8 hexagonal nanosheets and observed a strong SHG signal when exposing the samples to a 900 nm incident laser with varying powers. The fitting data of Cr_5Te_8 nanosheets shows a second-order correlation between the SHG signals and laser power [Fig. 10(b)], in which the strong SHG intensity confirms that the 2D Cr_5Te_8 material has the broken symmetry. Furthermore, the angle-resolved polarization-dependent SHG ($I = I_0\cos^2 3\theta$) of this nanosheet is shown in Fig. 10(c), which reveals the six-fold symmetry of Cr_5Te_8 is consistent with the crystal structure. He *et al.* [53] measured the SHG spectra of monolayer Cr_2S_3 nanosheets, as shown in Fig. 7(d). The SHG polarization with threefold symmetry is consistent with the Cr_2S_3 structure, and it is believed that its SHG signal originates from the interaction between the Cr_2S_3/air interface. At the Cr_2S_3/air interface, the surface potential field is composed of boundary conditions due to the structure of the material, and the interaction between the nonlinear electric dipole at the interface and the incident light contributes to the second harmonic generation. This interface interaction is localized at the boundary and decreases with the increase of the thickness of the 2D material. The SHG measurements are of extraordinary significance in the study of crystal structure symmetry, lattice orientation, and characterization of heterojunction. Additionally, it also enables the characterization of magnetically ordered structures, magnetic domains, and plays a crucial role in many new 2D magnetic materials [140, 141].

4.3.2 Electronic and optoelectronic devices of 2D CrX_n

In addition to their excellent magnetic properties, Cr-based chalcogenides have recently garnered attention for their electronic and optoelectronic properties. He *et al.* [53] built a 1.89 nm Cr_2S_3 field effect transistor (FET) device, which was found to exhibit typical p-type semiconductor behavior with on/off ratios up to 10^3. Zhang *et al.* [106] fabricated two-dimensional Cr_2S_3 transistors to study their electrical properties, and the schematic and optical images of the device are shown in Fig. 10(e). Noteworthy, the thickness-dependent variation in conductivity type is exhibited by this 2D Cr_2S_3 device, as depicted in Fig. 10(f), with a typical p-type conductivity behavior observed for 2.6 nm Cr_2S_3, bipolar type emerging (the thickness > 4.8 nm), and typical n-type (the thickness > 7.6 nm). The hole mobility of the 3.6 nm Cr_2S_3 is about 6.3×10^{-3} $cm^2 \cdot V^{-1} \cdot s^{-1}$, while the electron mobility of the 12.5 nm Cr_2S_3 reaches around 1.8 $cm^2 \cdot V^{-1} \cdot s^{-1}$. The large variation in conductivity type with thickness primarily arises from disparate vacancy concentrations of Cr atoms within the depleted Cr layer of Cr_2S_3. Subsequently, they fabricated lateral homojunctions of Cr_2S_3, as shown in Fig. 10(g), including p_m-ambipolar/n, p/ambipolar, ambipolar/n, and n_m-ambipolar/n homojunctions, which were able to enhance the field-effect mobility up to a factor of six in the original direction [105]. In addition, Cr_2S_3 thin films were prepared by Gao *et al.* [54] using a two-step CVD method exhibit p-type semiconductor properties, and the conductive behavior remains nearly unaffected by variations in thickness (from 1.9 to 4.9 nm). The hole mobility of Cr_2S_3 exhibited an increasing trend with the thickness, as the mobility increased from 0.08 to 2.41 $cm^2 \cdot V^{-1} \cdot s^{-1}$ when the thickness increased from 1.9 nm to 4.6 nm, while the on/off ratio rose from 10^1 to 10^2. Meanwhile, they used the same approach to synthesize Cr_2Se_3 thin films, which showed a positive correlation between current and the thickness of Cr_2Se_3. The films did not have gate-regulation properties at all thicknesses. Recently, Zhou *et al.* [144] successfully achieved heteroatom P-element doping of Cr_2S_3 nanosheets, resulting in typical n-type doping and significant surface passivation, which enhanced the resistivity by 10^4 times compared to the intrinsic Cr_2S_3 samples. In addition, Liu *et al.* [64] measured the electrical properties of 1T-CrS_2 using the four-terminal method from 2 nm to 15 nm, all of which exhibit n-type semiconductor properties. Meanwhile, owing to its 2D structure and high transparency window, as well as the capability to modulate field effect properties within the THz spectral range, it is postulated that 1T-CrS_2 exhibits potential applications in the realm of THz sensing and imaging.

Zhang *et al.* [142] firstly investigated the photodetectivity of Cr_2S_3 nanosheets and found the bandgap of Cr_2S_3 film is about 0.15 eV, indicating a typical narrow bandgap semiconductor and has a broader wavelength photoresponse. The schematic diagram of the Cr_2S_3 photodetector device is depicted in Fig. 10(h), in which the Cr/Au were used as the contact electrode. With the excitation light at the wavelengths of 520, 808, and 1550 nm, the device demonstrates high photoresponsivity values of 14.4, 6.0 and 2.0 $A \cdot W^{-1}$, respectively. Additionally, it exhibits high detectivity values of 4.0×10^{10} Jones, 1.7×10^{10} Jones, and 8.3×10^9 Jones at $V_{ds} = 0.1$ V, respectively, as shown in Fig. 10(i). Meanwhile, the Cr_2S_3 photodetector was measured to have a response rate t_r/t_d of about 1.7/1.65 s at 520 nm wavelength and a 3.28 nW laser power, as illustrated in Fig. 10(j). Li *et al.* [143] accomplished the doping of Cr_2S_3 with different concentrations of Se elements, where the conductivity and on/off ratio were strongly dependent on the doping concentration of Se, as shown in Fig. 10(k). When the Se doping concentration reached 2.05%, the room-temperature mobility of the Cr_2S_3 transistor was enhanced from 5.32×10^{-3} to 1.96×10^{-1} $cm^2 \cdot V^{-1} \cdot s^{-1}$. Moreover, the 2.05% Se-doped Cr_2S_3 exhibited excellent optoelectronic performance, as shown in Fig. 10(l). At an incident laser of 660 nm and 8.82 nW, the response rate of 2.05% Se-doped Cr_2S_3 device (t_r/t_d = 28/28 ms) was approximately 200 times faster than that of undoped Cr_2S_3 (t_r/t_d = 4.9/5.7 s). In addition, the maximum photoresponsivities of Cr_2S_3 and 2.05% Se-doped Cr_2S_3 devices were measured to be 3.23 and 10.41 $A \cdot W^{-1}$, respectively (an incident wavelength of 660 nm). And the corresponding detectivities were determined to be 1.05×10^{11} Jones and 2.37×10^{11} Jones.

In general, Cr-based chalcogenides transistor devices have excellent electrical properties such as mobility variation with thickness, sizable switching ratios, and thickness-dependent conductive behavior. Meanwhile, 2D Cr-based chalcogenides photodetectors are considered as the promising materials for future photodetection in the visible to near-infrared wavelength bands due to their narrow bandgap and other advantages, exhibiting a wide-band optical response, high detectivity and fast response speed. It is possible that the performance of Cr-based chalcogenides photodetectors can be significantly improved through elemental doping, heterojunction formation, and other material modifications as well as device surface and interface engineering [145–148].

5 Conclusions and perspective

In this article, we provide a comprehensive review of the structures, synthesis strategies, and exceptional physical properties of 2D Cr-based chalcogenides materials. Firstly, from a structural perspective, Cr-X chalcogenides possesses a distinctive interlayer CrX_2 intercalation structure that impacts numerous inherent novel properties. Therefore, it is of paramount importance to effectively

control the ratio of Cr atom intercalation in order to achieve precise modulation of the physical properties in 2D Cr-X systems. Our primary focus lies on exploring various nanosheet synthesis methods for these systems and examining the advantages offered by liquid-phase exfoliation, solution-based approaches, MBE, and CVD techniques for synthesizing different structured CrX_n nanosheets. Notably, considering that most Cr-X systems are non-layered materials, and particular emphasis is also placed on achieving controlled growth of such non-layered materials through van der Waals epitaxy method on substrates devoid of dangling bonds. The phase control of CrX_n nanosheets achieved through CVD is comprehensively analyzed, with particular emphasis on the influence of temperature, precursor type, and elemental doping on their phase regulation. Furthermore, a comprehensive summary is presented on the magnetic properties, electrical characteristics, and optoelectronic behavior of CrX_n nanosheets and their heterojunctions at room temperature, including their 2D ferromagnetism and antiferromagnetism, magnetic anisotropy, as well as tunable magnetic properties. Additionally, the unique electronic properties and wide-band optoelectronic detection capability arising from the narrow bandgap structure exhibited by semiconductor-characterized Cr_2S_3 nanosheets are discussed.

However, the growth and application of these materials are limited by several factors: (i) the van der Waals epitaxy of non-layered 2D CrX_n thin films has limitations, and the synthesis of non-layered materials is more prone to interfacial stress problems due to the presence of dangling bonds, and wafer-scale ultrathin single-crystal thin film growth is currently not feasible; (ii) considering the existence of surface dangling bonds in non-layered CrX_n materials, its surface defect density has a great influence on the properties of the material itself, how to realize the passivation of the surface dangling bonds in non-lamellar materials is also very important; (iii) currently, there is a paucity of studies on the heterojunctions of the Cr-X system, which should be integrated with the distinctive electrical and magnetic properties of Cr-X to fabricate novel heterojunction devices and further expand their application in transistors and spintronic devices; (iv) the utilization of ferromagnetic devices for CrXn nanosheets is still nascent, necessitating crucial device design for these 2D room-temperature ferromagnetic materials to be applied in nonvolatile storage and logic devices; (v) most Cr-X materials are semimetallic or metallic, precluding their use as switches for electronic devices and limiting their potential applications in electronic and optoelectronic devices, requiring the search for high- carrier mobility and long carrier lifetime of the 2D Cr-X semiconductors.

In conclusion, the synthesis and device applications of 2D Cr-based sulfides still hold significant untapped potential for exploration and possess substantial research value. This review comprehensively presents the theoretical and experimental advancements in 2D Cr-based chalcogenides, while also highlighting the primary challenges and proposing future research strategies for this promising 2D material, thereby providing valuable insights into its prospective research direction.

Declarations The authors declare that they have no competing interests and there are no conflicts.

Acknowledgements This work was financially supported by the Science and Technology Innovation Program of Hunan Province ("HuXiang Young Talents", Grant No. 2021RC3021), the Natural Science Foundation of Hunan Province, China (Grant No. 2021JJ40780), and the National Natural Science Foundation of China (Grant No. 51902346). This work was also supported by the Open Project Program of Shanxi Key Laboratory of Advanced Semiconductor Optoelectronic Devices and Integrated Systems (Grant No. 2023SZKF14).

References

1. K. S. Novoselov, A. K. Geim, S. V. Morozov, D. Jiang, Y. Zhang, S. V. Dubonos, I. V. Grigorieva, and A. A. Firsov, Electric field effect in atomically thin carbon films, *Science* 306(5696), 666 (2004)
2. O. Lopez-Sanchez, D. Lembke, M. Kayci, A. Radenovic, and A. Kis, Ultrasensitive photodetectors based on monolayer MoS_2, *Nat. Nanotechnol.* 8(7), 497 (2013)
3. A. A. Balandin, Thermal properties of graphene and nanostructured carbon materials, *Nat. Mater.* 10(8), 569 (2011)
4. M. W. Iqbal, M. Z. Iqbal, M. F. Khan, M. A. Shehzad, Y. Seo, J. H. Park, C. Hwang, and J. Eom, High-mobility and air-stable single-layer WS_2 field-effect transistors sandwiched between chemical vapor deposition-grown hexagonal BN films, *Sci. Rep.* 5(1), 10699 (2015)
5. N. Wang, Y. Song, L. Wang, K. Liu, and Y. Yang, Investigating the electrical properties of monolayer and bilayer h-BNs via atomic force microscopy, *Adv. Mater. Interfaces* 8(16), 2100447 (2021)
6. X. Wang, Q. Chen, C. Shen, J. Dai, C. Zhu, J. Zhang, Z. Wang, Q. Song, L. Wang, H. Li, Q. Wang, Z. Liu, Z. Luo, X. Huang, and W. Huang, Spatially controlled preparation of layered metallic-semiconducting metal chalcogenide heterostructures, *ACS Nano* 15(7), 12171 (2021)
7. Z. Zhao, W. Zhang, Y. Zhang, H. Hao, S. Zhang, L. Tong, B. Peng, and N. Liu, Tuning bandstructure of folded MoS_2 through fluid dynamics, *Nano Res.* 15(3), 2734 (2022)
8. F. Cui, Q. Feng, J. Hong, R. Wang, Y. Bai, X. Li, D. Liu, Y. Zhou, X. Liang, X. He, Z. Zhang, S. Liu, Z. Lei, Z. Liu, T. Zhai, and H. Xu, Synthesis of large-size 1T′ $ReS_{2x}Se_{2(1-x)}$ alloy monolayer with tunable bandgap and carrier type, *Adv. Mater.* 29(46), 1705015 (2017)

9. Y. Zhou, H. Jang, J. M. Woods, Y. Xie, P. Kumaravadivel, G. A. Pan, J. Liu, Y. Liu, D. G. Cahill, and J. J. Cha, Direct synthesis of large-scale WTe_2 Thin films with low Thermal conductivity, *Adv. Funct. Mater.* 27(8), 1605928 (2017)
10. C. H. Liu, Y. C. Chang, T. B. Norris, and Z. Zhong, Graphene photodetectors with ultra-broadband and high responsivity at room temperature, *Nat. Nanotechnol.* 9(4), 273 (2014)
11. D. Li, M. Chen, Z. Sun, P. Yu, Z. Liu, P. M. Ajayan, and Z. Zhang, Two-dimensional non-volatile programmable p–n junctions, *Nat. Nanotechnol.* 12(9), 901 (2017)
12. Y. Kim, S. Lee, J. G. Song, K. Y. Ko, W. J. Woo, S. W. Lee, M. Park, H. Lee, Z. Lee, H. Choi, W. H. Kim, J. Park, and H. Kim, H. Kim, 2D transition metal dichalcogenide heterostructures for p-and n-Type photovoltaic self-powered gas sensor, *Adv. Funct. Mater.* 30(43), 2003360 (2020)
13. B. Wang, H. Luo, X. Wang, E. Wang, Y. Sun, Y. C. Tsai, J. Dong, P. Liu, H. Li, Y. Xu, S. Tongay, K. Jiang, S. Fan, and K. Liu, Direct laser patterning of two-dimensional lateral transition metal disulfide-oxide-disulfide heterostructures for ultrasensitive sensors, *Nano Res.* 13(8), 2035 (2020)
14. A. Sebastian, R. Pendurthi, T. H. Choudhury, J. M. Redwing, and S. Das, Benchmarking monolayer MoS_2 and WS_2 field-effect transistors, *Nat. Commun.* 12(1), 693 (2021)
15. K. Li, C. Du, H. Gao, T. Yin, L. Zheng, J. Leng, and W. Wang, Ultrafast and polarization-sensitive ReS_2/$ReSe_2$ heterostructure photodetectors with ambipolar photoresponse, *ACS Appl. Mater. Interfaces* 14(29), 33589 (2022)
16. D. Wu, M. Xu, L. Zeng, Z. Shi, Y. Tian, X. J. Li, C. X. Shan, and J. Jie, *In situ* fabrication of $PdSe_2$/GaN Schottky junction for polarization-sensitive ultraviolet photodetection with high dichroic ratio, *ACS Nano* 16(4), 5545 (2022)
17. N. Li, Y. Wen, R. Cheng, L. Yin, F. Wang, J. Li, T. A. Shifa, L. Feng, Z. Wang, and J. He, Strongly coupled van der Waals heterostructures for high-performance infrared phototransistor, *Appl. Phys. Lett.* 114(10), 103501 (2019)
18. Y. She, Z. Wu, S. You, Q. Du, X. Chu, L. Niu, C. Ding, K. Zhang, L. Zhang, and S. Huang, Multiple-dimensionally controllable nucleation sites of two-dimensional WS_2/Bi_2Se_3 heterojunctions based on vapor growth, *ACS Appl. Mater. Interfaces* 13(13), 15518 (2021)
19. J. Chen, R. Guo, X. Wang, C. Zhu, G. Cao, L. You, R. Duan, C. Zhu, S. S. Hadke, X. Cao, T. Salim, P. J. S. Buenconsejo, M. Xu, X. Zhao, J. Zhou, Y. Deng, Q. Zeng, L. H. Wong, J. Chen, F. Liu, and Z. Liu, Solid-ionic memory in a van der Waals heterostructure, *ACS Nano* 16(1), 221 (2022)
20. F. Wu, H. Tian, Y. Shen, Z. Hou, J. Ren, G. Gou, Y. Sun, Y. Yang, and T. L. Ren, Vertical MoS_2 transistors with sub-1-nm gate lengths, *Nature* 603(7900), 259 (2022)
21. T. Li, W. Guo, L. Ma, W. Li, Z. Yu, Z. Han, S. Gao, L. Liu, D. Fan, Z. Wang, Y. Yang, W. Lin, Z. Luo, X. Chen, N. Dai, X. Tu, D. Pan, Y. Yao, P. Wang, Y. Nie, J. Wang, Y. Shi, and X. Wang, Epitaxial growth of wafer-scale molybdenum disulfide semiconductor single crystals on sapphire, *Nat. Nanotechnol.* 16(11), 1201 (2021)
22. P. C. Shen, C. Su, Y. Lin, A. S. Chou, C. C. Cheng, J. H. Park, M. H. Chiu, A. Y. Lu, H. L. Tang, M. M. Tavakoli, G. Pitner, X. Ji, Z. Cai, N. Mao, J. Wang, V. Tung, J. Li, J. Bokor, A. Zettl, C. I. Wu, T. Palacios, L. J. Li, and J. Kong, Ultralow contact resistance between semimetal and monolayer semiconductors, *Nature* 593(7858), 211 (2021)
23. H. Zheng, C. Huang, F. Lin, J. Fan, H. Liu, L. Zhang, C. Ma, C. Wang, Y. Zhu, and H. Yang, Two-dimensional van der Waals ferromagnetic thin film $CrTe_2$ with high Curie temperature and metallic conductivity, *Appl. Phys. Lett.* 122(2), 023103 (2023)
24. L. Qiu, Z. Wang, X. S. Ni, D. X. Yao, and Y. Hou, Electrically tunable Gilbert damping in van der Waals heterostructures of two-dimensional ferromagnetic metals and ferroelectrics, *Appl. Phys. Lett.* 122(10), 102402 (2023)
25. X. Zhang, W. Liu, W. Niu, Q. Lu, W. Wang, A. Sarikhani, X. Wu, C. Zhu, J. Sun, M. Vaninger, P. F. Miceli, J. Li, D. J. Singh, Y. S. Hor, Y. Zhao, C. Liu, L. He, R. Zhang, G. Bian, D. Yu, and Y. Xu, Self-intercalation tunable interlayer exchange coupling in a synthetic van der Waals antiferromagnet, *Adv. Funct. Mater.* 32(32), 2202977 (2022)
26. G. Xiao, W. Z. Xiao, Q. Chen, and L. Wang, Novel two-dimensional ferromagnetic materials CrX_2 (X = O, S, Se) with high Curie temperature, *J. Mater. Chem. C* 10(46), 17665 (2022)
27. Z. He, R. Peng, X. Feng, X. Xu, Y. Dai, B. Huang, and Y. Ma, Two-dimensional valleytronic semiconductor with spontaneous spin and valley polarization in single-layer Cr_2Se_3, *Phys. Rev. B* 104(7), 075105 (2021)
28. F. Chen, Y. Wang, W. Su, S. Ding, and L. Fu, Position-selective growth of 2D WS_2-based vertical heterostructures via a one-step CVD approach, *J. Phys. Chem. C* 123(50), 30519 (2019)
29. X. Guan, X. Yu, D. Periyanagounder, M. R. Benzigar, J. K. Huang, C. H. Lin, J. Kim, S. Singh, L. Hu, G. Liu, D. Li, J. H. He, F. Yan, Q. J. Wang, and T. Wu, Recent progress in short- to long-wave infrared photodetection using 2D materials and heterostructures, *Adv. Opt. Mater.* 9(4), 2001708 (2021)
30. H. G. Shin, H. S. Yoon, J. S. Kim, M. Kim, J. Y. Lim, S. Yu, J. H. Park, Y. Yi, T. Kim, S. C. Jun, and S. Im, Vertical and in-plane current devices using NbS_2/n-MoS_2 van der Waals Schottky junction and graphene contact, *Nano Lett.* 18(3), 1937 (2018)
31. B. Huang, G. Clark, E. Navarro-Moratalla, D. R. Klein, R. Cheng, K. L. Seyler, D. Zhong, E. Schmidgall, M. A. McGuire, D. H. Cobden, W. Yao, D. Xiao, P. Jarillo-Herrero, and X. Xu, Layer-dependent ferromagnetism in a van der Waals crystal down to the monolayer limit, *Nature* 546(7657), 270 (2017)
32. C. Gong, L. Li, Z. Li, H. Ji, A. Stern, Y. Xia, T. Cao, W. Bao, C. Wang, Y. Wang, Z. Q. Qiu, R. J. Cava, S. G. Louie, J. Xia, and X. Zhang, Discovery of intrinsic

ferromagnetism in two-dimensional van der Waals crystals, *Nature* 546(7657), 265 (2017)
33. Y. Deng, Y. Yu, Y. Song, J. Zhang, N. Z. Wang, Z. Sun, Y. Yi, Y. Z. Wu, S. Wu, J. Zhu, J. Wang, X. H. Chen, and Y. Zhang, Gate-tunable room-temperature ferromagnetism in two-dimensional Fe_3GeTe_2, *Nature* 563(7729), 94 (2018)
34. M. Bonilla, S. Kolekar, Y. Ma, H. C. Diaz, V. Kalappattil, R. Das, T. Eggers, H. R. Gutierrez, M. H. Phan, and M. Batzill, Strong room-temperature ferromagnetism in VSe_2 monolayers on van der Waals substrates, *Nat. Nanotechnol.* 13(4), 289 (2018)
35. L. Kang, C. Ye, X. Zhao, X. Zhou, J. Hu, Q. Li, D. Liu, C. M. Das, J. Yang, D. Hu, J. Chen, X. Cao, Y. Zhang, M. Xu, J. Di, D. Tian, P. Song, G. Kutty, Q. Zeng, Q. Fu, Y. Deng, J. Zhou, A. Ariando, F. Miao, G. Hong, Y. Huang, S. J. Pennycook, K. T. Yong, W. Ji, X. Renshaw Wang, and Z. Liu, Phase-controllable growth of ultrathin 2D magnetic FeTe crystals, *Nat. Commun.* 11(1), 3729 (2020)
36. Z. Fei, B. Huang, P. Malinowski, W. Wang, T. Song, J. Sanchez, W. Yao, D. Xiao, X. Zhu, A. F. May, W. Wu, D. H. Cobden, J. H. Chu, and X. Xu, Two-dimensional itinerant ferromagnetism in atomically thin Fe_3GeTe_2, *Nat. Mater.* 17(9), 778 (2018)
37. C. Zhang, C. Liu, J. Zhang, Y. Yuan, Y. Wen, Y. Li, D. Zheng, Q. Zhang, Z. Hou, G. Yin, K. Liu, Y. Peng, and X. X. Zhang, Room-temperature magnetic skyrmions and large topological Hall effect in chromium telluride engineered by self-intercalation, *Adv. Mater.* 35(1), 2205967 (2023)
38. X. Yang, X. Zhou, W. Feng, and Y. Yao, Tunable magneto-optical effect, anomalous Hall effect, and anomalous Nernst effect in the two-dimensional room-temperature ferromagnet 1T-$CrTe_2$, *Phys. Rev. B* 103(2), 024436 (2021)
39. F. Jellinek, The structures of the chromium sulphides, *Acta Crystallogr.* 10(10), 620 (1957)
40. A. Maignan, Y. Bréard, E. Guilmeau, and F. Gascoin, Transport, thermoelectric, and magnetic properties of a dense Cr_2S_3 ceramic, *J. Appl. Phys.* 112(1), 013716 (2012)
41. W. H. Xie, Y. Q. Xu, B. G. Liu, and D. G. Pettifor, Half-metallic ferromagnetism and structural stability of zincblende phases of the transition-metal chalcogenides, *Phys. Rev. Lett.* 91(3), 037204 (2003)
42. M. Anisha, M. Singh, R. Kumar, S. Srivastava, and K. Tankeshwar, Tuning of Thermoelectric performance of $CrSe_2$ material using dimension engineering, *J. Phys. Chem. Solids* 172, 111083 (2023)
43. M. G. Sreenivasan, J. F. Bi, K. L. Teo, and T. Liew, Systematic investigation of structural and magnetic properties in molecular beam epitaxial growth of metastable zinc-blende CrTe toward half-metallicity, *J. Appl. Phys.* 103(4), 043908 (2008)
44. A. L. Coughlin, D. Xie, X. Zhan, Y. Yao, L. Deng, H. Hewa-Walpitage, T. Bontke, C. W. Chu, Y. Li, J. Wang, H. A. Fertig, and S. Zhang, Van der Waals superstructure and twisting in self-intercalated magnet with near room-temperature perpendicular ferromagnetism, *Nano Lett.* 21(22), 9517 (2021)
45. Y. Sharma, P. Srivastava, A. Ghoshray, B. Bandyopadhyay, and C. Mazumdar, Electronic structure and magnetic properties of rhombohedral Cr_2S_3, *AIP Conf. Proc.* 1347(123), 123 (2011)
46. S. J. Zhang, J. M. Yan, F. Tang, J. Wu, W. Q. Dong, D. W. Zhang, F. S. Luo, L. Chen, Y. Fang, T. Zhang, Y. Chai, W. Zhao, X. Wang, and R. K. Zheng, Colossal magnetoresistance in Ti lightly doped Cr_2Se_3 single crystals with a layered structure, *ACS Appl. Mater. Interfaces* 13(49), 58949 (2021)
47. S. B. Chen, Z. Y. Zeng, X. R. Chen, and X. X. Yao, Strain-induced electronic structures, mechanical anisotropy, and piezoelectricity of transition-metal dichalcogenide monolayer CrS_2, *J. Appl. Phys.* 128(12), 125111 (2020)
48. S. Ebrahimi and B. Yarmand, Optimized optical band gap energy and Urbach tail of Cr_2S_3 thin films by Sn incorporation for optoelectronic applications, *Physica B* 593, 412292 (2020)
49. T. Zhang, X. Su, Y. Yan, W. Liu, T. Hu, C. Zhang, Z. Zhang, and X. Tang, Enhanced thermoelectric properties of codoped Cr_2Se_3: The distinct roles of transition metals and S, *ACS Appl. Mater. Interfaces* 10(26), 22389 (2018)
50. A. L. Coughlin, D. Xie, Y. Yao, X. Zhan, Q. Chen, H. Hewa-Walpitage, X. Zhang, H. Guo, H. Zhou, J. Lou, J. Wang, Y. S. Li, H. A. Fertig, and S. Zhang, Near degeneracy of magnetic phases in two-dimensional chromium telluride with enhanced perpendicular magnetic anisotropy, *ACS Nano* 14(11), 15256 (2020)
51. K. Niu, G. Qiu, C. Wang, D. Li, Y. Niu, S. Li, L. Kang, Y. Cai, M. Han, and J. Lin, Self-intercalated magnetic heterostructures in 2D chromium telluride, *Adv. Funct. Mater.* 33(2), 2208528 (2023)
52. W. Huang, L. Gan, H. Yang, N. Zhou, R. Wang, W. Wu, H. Li, Y. Ma, H. Zeng, and T. Zhai, Controlled synthesis of ultrathin 2D β-In_2S_3 with broadband photoresponse by chemical vapor deposition, *Adv. Funct. Mater.* 27(36), 1702448 (2017)
53. J. Chu, Y. Zhang, Y. Wen, R. Qiao, C. Wu, P. He, L. Yin, R. Cheng, F. Wang, Z. Wang, J. Xiong, Y. Li, and J. He, Sub-millimeter-scale growth of one-unit-cell-thick ferrimagnetic Cr_2S_3 nanosheets, *Nano Lett.* 19(3), 2154 (2019)
54. B. Yao, W. Liu, X. Zhou, J. Yang, X. Huang, Z. Fu, G. Yuan, Y. Nie, Y. Dai, J. Xu, and L. Gao, Growth of wafer-scale chromium sulphide and selenide semiconductor films, *J. Phys.: Condens. Matter* 35(33), 335302 (2023)
55. Z. Jin, Z. Ji, Y. Zhong, Y. Jin, X. Hu, X. Zhang, L. Zhu, X. Huang, T. Li, X. Cai, and L. Zhou, Controlled synthesis of a two-dimensional non-van der Waals ferromagnet toward a magnetic Moire superlattice, *ACS Nano* 16(5), 7572 (2022)
56. N. D. Mermin and H. Wagner, Absence of ferromagnetism or antiferromagnetism in one- or two-dimensional isotropic Heisenberg models, *Phys. Rev. Lett.* 17(22), 1133 (1966)
57. Y. Gebredingle, M. Joe, and C. Lee, First-principles calculations of the spin-dependent electronic structure and strain tunability in 2D non-van der Waals

chromium chalcogenides Cr_2X_3 (X = S, Se, Te): Implications for spintronics applications, *ACS Appl. Nano Mater.* 5(8), 10383 (2022)
58. H. Groß, D. Groeneveld, M. Poschmann, U. Schürmann, J. D. König, W. Bensch, J. Wöllenstein, and L. Kienle, About the impact of defect phases on the thermoelectric properties of $Cr_3S_{4-x}Se_x$, *Adv. Eng. Mater.* 25(9), 2201505 (2023)
59. N. Kang, W. Wan, Y. Ge, and Y. Liu, Diverse magnetism in stable and metastable structures of CrTe, *Front. Phys.* 16(6), 63506 (2021)
60. Y. Guo, L. Kang, S. Yu, J. Yang, X. Qi, Z. Zhang, and Z. Liu, CVD growth of large-scale and highly crystalline 2D chromium telluride nanoflakes, *ChemNanoMat* 7(3), 323 (2021)
61. Y. Zhang, J. Chu, L. Yin, T. A. Shifa, Z. Cheng, R. Cheng, F. Wang, Y. Wen, X. Zhan, Z. Wang, and J. He, Ultrathin magnetic 2D single-crystal CrSe, *Adv. Mater.* 31(19), 1900056 (2019)
62. M. R. Habib, S. Wang, W. Wang, H. Xiao, S. M. Obaidulla, A. Gayen, Y. Khan, H. Chen, and M. Xu, Electronic properties of polymorphic two-dimensional layered chromium disulphide, *Nanoscale* 11(42), 20123 (2019)
63. P. Li, C. Xu, and W. Luo, Layer-independent ferromagnetic insulators in a new structural phase of Cr_2S_3, *Phys. Rev. Mater.* 6(5), 054006 (2022)
64. G. K. Rajendran Nair, A. Abdelaziem, X. Zhao, X. Wang, D. Hu, Y. Wu, C. Xun, F. Le Goualher, C. Zhu, P. L. P. Yin, V. Valsaraj, T. Salim, L. Ke, and Z. Liu, Chemical vapor deposition of phase-pure 2D 1T-CrS_2, *Phys. Status Solidi Rapid Res. Lett.* 16(4), 2100495 (2022)
65. S. Zhou, R. Wang, J. Han, D. Wang, H. Li, L. Gan, and T. Zhai, Ultrathin non-van der Waals magnetic rhombohedral Cr_2S_3: Space-confined chemical vapor deposition synthesis and raman scattering investigation, *Adv. Funct. Mater.* 29(3), 1805880 (2019)
66. T. A. Shifa, R. Mazzaro, V. Morandi, and A. Vomiero, Controllable synthesis of 2D nonlayered Cr_2S_3 nanosheets and their electrocatalytic activity toward oxygen evolution reaction, *Front. Chem. Eng.* 3, 703812 (2021)
67. M. G. Moinuddin, S. Srinivasan, and S. K. Sharma, Probing ferrimagnetic semiconductor with enhanced negative magnetoresistance: 2D chromium sulfide, *Adv. Electron. Mater.* 7(9), 2001116 (2021)
68. S. Kobayashi, N. Katayama, T. Manjo, H. Ueda, C. Michioka, J. Sugiyama, Y. Sassa, O. K. Forslund, M. Mansson, K. Yoshimura, and H. Sawa, Linear trimer formation with antiferromagnetic ordering in 1T-$CrSe_2$ originating from Peierls-like instabilities and interlayer Se–Se interactions, *Inorg. Chem.* 58(21), 14304 (2019)
69. X. Zhu, L. Wong, X. Fan, J. Zhao, Y. Zhou, and F. Ouyang, Role of the spatial distribution of gas flow for tuning the vertical/planar growth of nonlayered two-dimensional nanoplates, *Cryst. Growth Des.* 22(1), 763 (2022)
70. D. Zhang, C. Yi, C. Ge, W. Shu, B. Li, X. Duan, A. Pan, and X. Wang, Controlled vapor growth of 2D magnetic Cr_2Se_3 and its magnetic proximity effect in heterostructures, *Chin. Phys. B* 30(9), 097601 (2021)
71. S. Bai, S. Tang, M. Wu, D. Luo, J. Zhang, D. Wan, and X. Li, Chromium ditelluride monolayer: A novel promising 2H phase thermoelectric material with direct bandgap and ultralow lattice thermal conductivity, *J. Alloys Compd.* 930, 167485 (2023)
72. Y. Wang, S. Kajihara, H. Matsuoka, B. K. Saika, K. Yamagami, Y. Takeda, H. Wadati, K. Ishizaka, Y. Iwasa, and M. Nakano, Layer-number-independent two-dimensional ferromagnetism in Cr_3Te_4, *Nano Lett.* 22(24), 9964 (2022)
73. A. Purbawati, S. Sarkar, S. Pairis, M. Kostka, A. Hadj-Azzem, D. Dufeu, P. Singh, D. Bourgault, M. Nuñez-Regueiro, J. Vogel, J. Renard, L. Marty, F. Fabre, A. Finco, V. Jacques, L. Ren, V. Tiwari, C. Robert, X. Marie, N. Bendiab, N. Rougemaille, and J. Coraux, Stability of the in-plane room temperature van der waals ferromagnet chromium ditelluride and its conversion to chromium-interleaved $CrTe_2$ compounds, *ACS Appl. Electron. Mater.* 5(2), 764 (2023)
74. Y. Wen, Z. Liu, Y. Zhang, C. Xia, B. Zhai, X. Zhang, G. Zhai, C. Shen, P. He, R. Cheng, L. Yin, Y. Yao, M. Getaye Sendeku, Z. Wang, X. Ye, C. Liu, C. Jiang, C. Shan, Y. Long, and J. He, Tunable room-temperature ferromagnetism in two-dimensional Cr_2Te_3, *Nano Lett.* 20(5), 3130 (2020)
75. B. Li, X. Deng, W. Shu, X. Cheng, Q. Qian, Z. Wan, B. Zhao, X. Shen, R. Wu, S. Shi, H. Zhang, Z. Zhang, X. Yang, J. Zhang, M. Zhong, Q. Xia, J. Li, Y. Liu, L. Liao, Y. Ye, L. Dai, Y. Peng, B. Li, and X. Duan, Air-stable ultrathin Cr_3Te_4 nanosheets with thickness-dependent magnetic biskyrmions, *Mater. Today* 57, 66 (2022)
76. Z. W. Lu, S. B. Qiu, W. Q. Xie, X. B. Yang, and Y. J. Zhao, Theoretical study of strain induced magnetic transition of single-layer $CrTe_3$, *J. Appl. Phys.* 127(3), 033903 (2020)
77. H. Liu, J. Fan, H. Zheng, J. Wang, C. Ma, H. Wang, L. Zhang, C. Wang, Y. Zhu, and H. Yang, Magnetic properties and critical behavior of quasi-2D layered Cr_4Te_5 thin film, *Front. Phys.* 18(1), 13302 (2023)
78. W. Wang, J. Fan, H. Liu, H. Zheng, C. Ma, L. Zhang, Y. Sun, C. Wang, Y. Zhu, and H. Yang, Fabrication and magnetic-electronic properties of van der Waals Cr_4Te_5 ferromagnetic films, *CrystEngComm* 24(3), 674 (2022)
79. J. Liu, B. Ding, J. Liang, X. Li, Y. Yao, and W. Wang, Magnetic skyrmionic bubbles at room temperature and sign reversal of the topological Hall effect in a layered ferromagnet $Cr_{0.87}Te$, *ACS Nano* 16(9), 13911 (2022)
80. M. Huang, L. Gao, Y. Zhang, X. Lei, G. Hu, J. Xiang, H. Zeng, X. Fu, Z. Zhang, G. Chai, Y. Peng, Y. Lu, H. Du, G. Chen, J. Zang, and B. Xiang, Possible topological Hall effect above room temperature in layered $Cr_{1.2}Te_2$ ferromagnet, *Nano Lett.* 21(10), 4280 (2021)
81. J. Yan, X. Luo, G. Lin, F. Chen, J. Gao, Y. Sun, L. Hu, P. Tong, W. Song, Z. Sheng, W. Lu, X. Zhu, and Y. Sun, Anomalous Hall effect of the quasi-two-dimensional weak itinerant ferromagnet $Cr_{4.14}Te_8$, *Europhys. Lett.* 124(6), 67005 (2019)
82. J. Wang, X. Xu, T. Cheng, L. Gu, R. Qiao, Z. Liang,

D. Ding, H. Hong, P. Zheng, Z. Zhang, Z. Zhang, S. Zhang, G. Cui, C. Chang, C. Huang, J. Qi, J. Liang, C. Liu, Y. Zuo, G. Xue, X. Fang, J. Tian, M. Wu, Y. Guo, Z. Yao, Q. Jiao, L. Liu, P. Gao, Q. Li, R. Yang, G. Zhang, Z. Tang, D. Yu, E. Wang, J. Lu, Y. Zhao, S. Wu, F. Ding, and K. Liu, Dual-coupling-guided epitaxial growth of wafer-scale single-crystal WS_2 monolayer on vicinal a-plane sapphire, *Nat. Nanotechnol.* 17(1), 33 (2022)

83. G. Eda, H. Yamaguchi, D. Voiry, T. Fujita, M. Chen, and M. Chhowalla, Photoluminescence from chemically exfoliated MoS_2, *Nano Lett.* 11(12), 5111 (2011)
84. J. Zheng, H. Zhang, S. Dong, Y. Liu, C. Tai Nai, H. Suk Shin, H. Young Jeong, B. Liu, and K. Ping Loh, High yield exfoliation of two-dimensional chalcogenides using sodium naphthalenide, *Nat. Commun.* 5(1), 2995 (2014)
85. J. N. L. Coleman, M. Lotya, A. O'Neill, S. D. Bergin, P. J. King, U. Khan, K. Young, A. Gaucher, S. De, R. J. Smith, I. V. Shvets, S. K. Arora, G. Stanton, H. Y. Kim, K. Lee, G. T. Kim, G. S. Duesberg, T. Hallam, J. J. Boland, J. J. Wang, J. F. Donegan, J. C. Grunlan, G. Moriarty, A. Shmeliov, R. J. Nicholls, J. M. Perkins, E. M. Grieveson, K. Theuwissen, D. W. McComb, P. D. Nellist, and V. Nicolosi, Two-Dimensional Nanosheets Produced by Liquid Exfoliation of Layered Materials, *Science* 331(6017), 568 (2011)
86. M. Huang, S. Wang, Z. Wang, P. Liu, J. Xiang, C. Feng, X. Wang, Z. Zhang, Z. Wen, H. Xu, G. Yu, Y. Lu, W. Zhao, S. A. Yang, D. Hou, and B. Xiang, Colossal anomalous Hall effect in ferromagnetic van der Waals $CrTe_2$, *ACS Nano* 15(6), 9759 (2021)
87. X. Sun, W. Li, X. Wang, Q. Sui, T. Zhang, Z. Wang, L. Liu, D. Li, S. Feng, S. Zhong, H. Wang, V. Bouchiat, M. Nunez Regueiro, N. Rougemaille, J. Coraux, A. Purbawati, A. Hadj-Azzem, Z. Wang, B. Dong, X. Wu, T. Yang, G. Yu, B. Wang, Z. Han, X. Han, and Z. Zhang, Room temperature ferromagnetism in ultra-thin van der Waals crystals of 1T-$CrTe_2$, *Nano Res.* 13(12), 3358 (2020)
88. M. Huang, Z. Ma, S. Wang, S. Li, M. Li, J. Xiang, P. Liu, G. Hu, Z. Zhang, Z. Sun, Y. Lu, Z. Sheng, G. Chen, Y.-L. Chueh, S. A. Yang, B. Xiang, Significant perpendicular magnetic anisotropy in room-temperature layered ferromagnet of Cr-intercalated $CrTe_2$, *2D Mater.* 8(3), 031003 (2021)
89. W. Hussain, A. Badshah, R. A. Hussain, Imtiaz-ud-Din, M. A. Aleem, A. Bahadur, S. Iqbal, M. U. Farooq, and H. Ali, Photocatalytic applications of Cr_2S_3 synthesized from single and multi-source precursors, *Mater. Chem. Phys.* 194, 345 (2017)
90. S. Ramaraj, S. Mani, S. M. Chen, S. Palanisamy, V. Velusamy, J. M. Hall, T. W. Chen, and T. W. Tseng, Hydrothermal synthesis of Cr_2Se_3 hexagons for sensitive and low-level detection of 4-nitrophenol in water, *Sci. Rep.* 8(1), 4839 (2018)
91. X. Zhang, Q. Lu, W. Liu, W. Niu, J. Sun, J. Cook, M. Vaninger, P. F. Miceli, D. J. Singh, S. W. Lian, T. R. Chang, X. He, J. Du, L. He, R. Zhang, G. Bian, and Y. Xu, Room-temperature intrinsic ferromagnetism in epitaxial $CrTe_2$ ultrathin films, *Nat. Commun.* 12(1), 2492 (2021)
92. M. Liu, Y. L. Huang, J. Gou, Q. Liang, R. Chua, S. Arramel, S. Duan, L. Zhang, L. L. Cai, X. Yu, D. Zhong, W. Zhang, and A. T. S. Wee, Diverse structures and magnetic properties in nonlayered monolayer chromium selenide, *J. Phys. Chem. Lett.* 12(32), 7752 (2021)
93. A. Koma, Van der Waals epitaxy for highly lattice mismatched systems, *J. Cryst. Growth* 201–202, 236 (1999)
94. C. Chen, X. Chen, C. Wu, X. Wang, Y. Ping, X. Wei, X. Zhou, J. Lu, L. Zhu, J. Zhou, T. Zhai, J. Han, and H. Xu, Air-stable 2D Cr_5Te_8 nanosheets with thickness-tunable ferromagnetism, *Adv. Mater.* 34(2), 2107512 (2022)
95. Q. Tang, C. Liu, B. Zhang, and W. Jie, Synthesis of sub-micro-flakes $CrSe_2$ on glass and (110) Si substrates by solvothermal method, *J. Solid State Chem.* 262, 53 (2018)
96. I. A. Kariper, Synthesis and characterization of CrSe thin film produced via chemical bath deposition, *Opt. Rev.* 24(2), 139 (2017)
97. F. M. Tezel and İ. A. Kariper, A new process to synthesize CrSe thin films with nanosize by CBD method, *Mater. Res. Express* 6(3), 036412 (2018)
98. S. Liu, X. Yuan, Y. Zou, Y. Sheng, C. Huang, E. Zhang, J. Ling, Y. Liu, W. Wang, C. Zhang, J. Zou, K. Wang, and F. Xiu, Wafer-scale two-dimensional ferromagnetic Fe_3GeTe_2 thin films grown by molecular beam epitaxy, *npj 2D Mater. Appl.* 1(1), 30 (2017)
99. S. M. Poh, X. Zhao, S. J. R. Tan, D. Fu, W. Fei, L. Chu, D. Jiadong, W. Zhou, S. J. Pennycook, A. H. Castro Neto, and K. P. Loh, Molecular beam epitaxy of highly crystalline $MoSe_2$ on hexagonal boron nitride, *ACS Nano* 12(8), 7562 (2018)
100. A. Roy, S. Guchhait, R. Dey, T. Pramanik, C. C. Hsieh, A. Rai, and S. K. Banerjee, Perpendicular magnetic anisotropy and spin glass-like behavior in molecular beam epitaxy grown chromium telluride thin films, *ACS Nano* 9(4), 3772 (2015)
101. C. Wang, B. Zhang, B. You, S. K. Lok, S. K. Chan, X. X. Zhang, G. K. L. Wong, and I. K. Sou, Molecular-beam-epitaxy-grown CrSe/Fe bilayer on GaAs(100) substrate, *J. Appl. Phys.* 102(8), 083901 (2007)
102. H. Li, L. Wang, J. Chen, T. Yu, L. Zhou, Y. Qiu, H. He, F. Ye, I. K. Sou, and G. Wang, Molecular beam epitaxy grown Cr_2Te_3 thin films with tunable Curie temperatures for spintronic devices, *ACS Appl. Nano Mater.* 2(11), 6809 (2019)
103. Y. Zuo, C. Liu, L. Ding, R. Qiao, J. Tian, C. Liu, Q. Wang, G. Xue, Y. You, Q. Guo, J. Wang, Y. Fu, K. Liu, X. Zhou, H. Hong, M. Wu, X. Lu, R. Yang, G. Zhang, D. Yu, E. Wang, X. Bai, F. Ding, and K. Liu, Robust growth of two-dimensional metal dichalcogenides and their alloys by active chalcogen monomer supply, *Nat. Commun.* 13(1), 1007 (2022)
104. P. Yang, S. Zhang, S. Pan, B. Tang, Y. Liang, X. Zhao, Z. Zhang, J. Shi, Y. Huan, Y. Shi, S. J. Pennycook, Z. Ren, G. Zhang, Q. Chen, X. Zou, Z. Liu, and Y. Zhang, Epitaxial growth ofcentimeter-scale single-crystal MoS_2 monolayer on Au(111), *ACS Nano* 14(4), 5036 (2020)

105. F. Cui, X. Zhao, B. Tang, L. Zhu, Y. Huan, Q. Chen, Z. Liu, and Y. Zhang, Epitaxial growth of step-like Cr_2S_3 lateral homojunctions towards versatile conduction polarities and enhanced transistor performances, *Small* 18(4), 2105744 (2021)
106. F. Cui, X. Zhao, J. Xu, B. Tang, Q. Shang, J. Shi, Y. Huan, J. Liao, Q. Chen, Y. Hou, Q. Zhang, S. J. Pennycook, and Y. Zhang, Controlled growth and thickness-dependent conduction-type transition of 2D ferrimagnetic Cr_2S_3 semiconductors, *Adv. Mater.* 32(4), 1905896 (2020)
107. X. Zhang, B. Wang, Y. Guo, Y. Zhang, Y. Chen, and J. Wang, High Curie temperature and intrinsic ferromagnetic half-metallicity in two-dimensional Cr_3X_4 (X = S, Se, Te) nanosheets, *Nanoscale Horiz.* 4(4), 859 (2019)
108. C. Ma, J. R. Beckett, and G. R. Rossman, Murchisite, Cr_5S_6, a new mineral from the Murchison meteorite, *Am. Mineral.* 96(11–12), 1905 (2011)
109. B. Li, Z. Wan, C. Wang, P. Chen, B. Huang, X. Cheng, Q. Qian, J. Li, Z. Zhang, G. Sun, B. Zhao, H. Ma, R. Wu, Z. Wei, Y. Liu, L. Liao, Y. Ye, Y. Huang, X. Xu, X. Duan, W. Ji, and X. Duan, Van der Waals epitaxial growth of air-stable $CrSe_2$ nanosheets with thickness-tunable magnetic order, *Nat. Mater.* 20(6), 818 (2021)
110. Q. Wu, R. Liu, Z. Qiu, D. Li, J. Li, X. Wang, and G. Ding, Cr_3X_4 (X = Se, Te) monolayers as a new platform to realize robust spin filters, spin diodes and spin valves, *Phys. Chem. Chem. Phys.* 24(40), 24873 (2022)
111. D. Zhao, L. Zhang, I. A. Malik, M. Liao, W. Cui, X. Cai, C. Zheng, L. Li, X. Hu, D. Zhang, J. Zhang, X. Chen, W. Jiang, and Q. Xue, Observation of unconventional anomalous Hall effect in epitaxial CrTe thin films, *Nano Res.* 11(6), 3116 (2018)
112. M. Wang, L. Kang, J. Su, L. Zhang, H. Dai, H. Cheng, X. Han, T. Zhai, Z. Liu, and J. Han, Two-dimensional ferromagnetism in CrTe flakes down to atomically thin layers, *Nanoscale* 12(31), 16427 (2020)
113. L. Meng, Z. Zhou, M. Xu, S. Yang, K. Si, L. Liu, X. Wang, H. Jiang, B. Li, P. Qin, P. Zhang, J. Wang, Z. Liu, P. Tang, Y. Ye, W. Zhou, L. Bao, H. J. Gao, and Y. Gong, Anomalous thickness dependence of Curie temperature in air-stable two-dimensional ferromagnetic 1T-$CrTe_2$ grown by chemical vapor deposition, *Nat. Commun.* 12(1), 809 (2021)
114. J. J. Xian, C. Wang, J. H. Nie, R. Li, M. Han, J. Lin, W. H. Zhang, Z. Y. Liu, Z. M. Zhang, M. P. Miao, Y. Yi, S. Wu, X. Chen, J. Han, Z. Xia, W. Ji, and Y. S. Fu, Spin mapping of intralayer antiferromagnetism and field-induced spin reorientation in monolayer $CrTe_2$, *Nat. Commun.* 13(1), 257 (2022)
115. R. Chua, J. Zhou, X. Yu, W. Yu, J. Gou, R. Zhu, L. Zhang, M. Liu, M. B. H. Breese, W. Chen, K. P. Loh, Y. P. Feng, M. Yang, Y. L. Huang, and A. T. S. Wee, Room temperature ferromagnetism of monolayer chromium telluride with perpendicular magnetic anisotropy, *Adv. Mater.* 33(42), 2103360 (2021)
116. R. Li, J. H. Nie, J. J. Xian, J. W. Zhou, Y. Lu, M. P. Miao, W. H. Zhang, and Y. S. Fu, Planar heterojunction of ultrathin $CrTe_3$ and $CrTe_2$ van der Waals magnet, *ACS Nano* 16(3), 4348 (2022)
117. C. L. Liu, Y. T. Tseng, C. W. Huang, H. Y. Lo, A. Y. Hou, C. H. Wang, A. Yasuhara, and W. W. Wu, Atomic imaging and thermally induced dynamic structural evolution of two-dimensional Cr_2S_3, *Nano Lett.* 22(19), 7944 (2022)
118. W. Zhou, M. Chen, C. Yuan, H. Huang, J. Zhang, Y. Wu, X. Zheng, J. Shen, G. Wang, S. Wang, and B. Shen, Antiferromagnetic phase induced by nitrogen doping in 2D Cr_2S_3, *Materials (Basel)* 15(5), 1716 (2022)
119. H. Yang, A. Wu, H. Yi, W. Cao, J. Yao, G. Yang, and Y. C. Zou, Atomic scale insights into the epitaxial growth mechanism of 2D Cr_3Te_4 on mica, *Nanoscale Adv.* 5(3), 693 (2023)
120. Y. Guo, L. Zhao, and D. Zheng, Theoretical investigation on the electronic structure of new InSe/CrS_2 van der Waals heterostructure, *J. Mater. Res.* 37(13), 2157 (2022)
121. S. Zhao, X. Zhang, and J. Cao, Mechanistic study of CrS_2/BP as a direct Z-scheme heterojunction for photocatalyst of splitting water under biaxial strain, *Catl. Lett.*, doi: 10.1007/s10562-022-04224-8 (2022)
122. C. Jiang, Z. Yang, W. Xiong, and F. Wang, Effect of strain engineering on magnetism-induced valley splitting in WSe_2 based on the WSe_2/$CrSe_2$ heterojunction, *Appl. Phys. Lett.* 119(16), 162101 (2021)
123. Y. Ou, W. Yanez, R. Xiao, M. Stanley, S. Ghosh, B. Zheng, W. Jiang, Y. S. Huang, T. Pillsbury, A. Richardella, C. Liu, T. Low, V. H. Crespi, K. A. Mkhoyan, and N. Samarth, $ZrTe_2$/$CrTe_2$: An epitaxial van der Waals platform for spintronics, *Nat. Commun.* 13(1), 2972 (2022)
124. X. Zhang, S. C. Ambhire, Q. Lu, W. Niu, J. Cook, J. S. Jiang, D. Hong, L. Alahmed, L. He, R. Zhang, Y. Xu, S. S. Zhang, P. Li, and G. Bian, Giant topological Hall effect in van der Waals heterostructures of $CrTe_2$/Bi_2Te_3, *ACS Nano* 15(10), 15710 (2021)
125. J. Yao, H. Wang, B. Yuan, Z. Hu, C. Wu, and A. Zhao, Ultrathin van der Waals antiferromagnet $CrTe_3$ for fabrication of in-plane $CrTe_3$/$CrTe_2$ monolayer magnetic heterostructures, *Adv. Mater.* 34(23), 2200236 (2022)
126. J. Chen, L. Wang, M. Zhang, L. Zhou, R. Zhang, L. Jin, X. Wang, H. Qin, Y. Qiu, J. Mei, F. Ye, B. Xi, H. He, B. Li, and G. Wang, Evidence for magnetic skyrmions at the interface of ferromagnet/topological-insulator heterostructures, *Nano Lett.* 19(9), 6144 (2019)
127. J. Matsuno, N. Ogawa, K. Yasuda, F. Kagawa, W. Koshibae, N. Nagaosa, Y. Tokura, and M. Kawasaki, Interface-driven topological Hall effect in $SrRuO_3$–$SrIrO_3$ bilayer, *Sci. Adv.* 2(7), e1600304 (2016)
128. A. Soumyanarayanan, M. Raju, A. L. Gonzalez Oyarce, A. K. C. Tan, M. Y. Im, A. P. Petrović, P. Ho, K. H. Khoo, M. Tran, C. K. Gan, F. Ernult, and C. Panagopoulos, Tunable room-temperature magnetic skyrmions in Ir/Fe/Co/Pt multilayers, *Nat. Mater.* 16(9), 898 (2017)
129. Z. Zhang, J. Shang, C. Jiang, A. Rasmita, W. Gao, and T. Yu, Direct photoluminescence probing of ferro-

magnetism in monolayer two-dimensional $CrBr_3$, *Nano Lett.* 19(5), 3138 (2019)

130. L. Wu, L. Zhou, X. Zhou, C. Wang, and W. Ji, In-plane epitaxy-strain-tuning intralayer and interlayer magnetic coupling in $CrSe_2$ and $CrTe_2$ monolayers and bilayers, *Phys. Rev. B* 106(8), L081401 (2022)
131. J. H. Jeon, H. R. Na, H. Kim, S. Lee, S. Song, J. Kim, S. Park, J. Kim, H. Noh, G. Kim, S. K. Jerng, and S. H. Chun, Emergent topological Hall effect from exchange coupling in ferromagnetic Cr_2Te_3/noncoplanar antiferromagnetic Cr_2Se_3 bilayers, *ACS Nano* 16(6), 8974 (2022)
132. Y. Fujisawa, M. Pardo-Almanza, J. Garland, K. Yamagami, X. Zhu, X. Chen, K. Araki, T. Takeda, M. Kobayashi, Y. Takeda, C. H. Hsu, F. C. Chuang, R. Laskowski, K. H. Khoo, A. Soumyanarayanan, and Y. Okada, Tailoring magnetism in self-intercalated $Cr_{1+\delta}Te_2$ epitaxial films, *Phys. Rev. Mater.* 4(11), 114001 (2020)
133. F. Yu, Y. Yin, G. Liu, Q. Tian, Q. Meng, W. Zhao, K. Wang, C. Wang, S. Yang, D. Wu, X. Wan, and Y. Zhang, Thickness-dependent structural phase transition and self-intercalation of two-dimensional ferromagnetic chromium telluride thin films, *Appl. Phys. Lett.* 120(26), 261602 (2022)
134. J. Zhong, M. Wang, T. Liu, Y. Zhao, X. Xu, S. Zhou, J. Han, L. Gan, and T. Zhai, Strain-sensitive ferromagnetic two-dimensional Cr_2Te_3, *Nano Res.* 15(2), 1254 (2022)
135. H. Chi, Y. Ou, T. B. Eldred, W. Gao, S. Kwon, J. Murray, M. Dreyer, R. E. Butera, A. C. Foucher, H. Ambaye, J. Keum, A. T. Greenberg, Y. Liu, M. R. Neupane, G. J. de Coster, O. A. Vail, P. J. Taylor, P. A. Folkes, C. Rong, G. Yin, R. K. Lake, F. M. Ross, V. Lauter, D. Heiman, and J. S. Moodera, Strain-tunable Berry curvature in quasi-two-dimensional chromium telluride, *Nat. Commun.* 14(1), 3222 (2023)
136. Q. Q. Li, S. Li, D. Wu, Z. K. Ding, X. H. Cao, L. Huang, H. Pan, B. Li, K. Q. Chen, and X. D. Duan, Magnetic properties manipulation of $CrTe_2$ bilayer through strain and self-intercalation, *Appl. Phys. Lett.* 119(16), 162402 (2021)
137. X. Zhu, H. Liu, L. Liu, L. Ren, W. Li, L. Fang, X. Chen, L. Xie, Y. Jing, J. Chen, S. Liu, F. Ouyang, Y. Zhou, and X. Xiong, Spin glass state in chemical vapor-deposited crystalline Cr_2Se_3 nanosheets, *Chem. Mater.* 33(10), 3851 (2021)
138. S. Sun, J. Liang, R. Liu, W. Shen, H. Wu, M. Tian, L. Cao, Y. Yang, Z. Huang, W. Lin, J. Du, Z. Ni, Y. Xu, Q. Chen, and Y. Zhai, Anisotropic magnetoresistance in room temperature ferromagnetic single crystal CrTe flake, *J. Alloys Compd.* 890, 161818 (2022)
139. F. S. Luo, J. S. Ying, T. W. Chen, F. Tang, D. W. Zhang, W. Q. Dong, Y. Zhang, S. S. Li, Y. Fang, and R. K. Zheng, Anomalous Hall effect and anisotropic magnetoresistance of molecular beam epitaxy grown Cr_2Te_3 thin films, *J. Cryst. Growth* 582, 126541 (2022)
140. S. A. Denev, T. T. A. Lummen, E. Barnes, A. Kumar, and V. Gopalan, Probing ferroelectrics using optical second harmonic generation, *J. Am. Ceram. Soc.* 94(9), 2699 (2011)
141. R. Zhang, W. Ruan, J. Yu, L. Gao, H. Berger, L. Forró, K. Watanabe, T. Taniguchi, A. Ranjbar, R. V. Belosludov, T. D. Kühne, M. S. Bahramy, and X. Xi, Second-harmonic generation in atomically thin 1T-$TiSe_2$ and its possible origin from charge density wave transitions, *Phys. Rev. B* 105(8), 085409 (2022)
142. L. Xie, J. Wang, J. Li, C. Li, Y. Zhang, B. Zhu, Y. Guo, Z. Wang, and K. Zhang, An atomically thin air-stable narrow-gap semiconductor Cr_2S_3 for broadband photodetection with high responsivity, *Adv. Electron. Mater.* 7(7), 2000962 (2021)
143. X. Zhou, C. Liu, L. Song, H. Zhang, Z. Huang, C. He, B. Li, X. Lin, Z. Zhang, S. Shi, D. Shen, R. Song, J. Li, X. Liu, X. Zou, L. Huang, L. Liao, X. Duan, and B. Li, Promoting the optoelectronic and ferromagnetic properties of Cr_2S_3 nanosheets via Se doping, *Sci. China Phys. Mech.* 65(7), 276811 (2022)
144. X. Fan, L. Zou, W. Chu, L. Wang, and Y. Zhou, Synthesis of high resistive two-dimensional nonlayered Cr_2S_3 nanoflakes with stable phosphorus dopants by chemical vapor deposition, *Appl. Phys. Lett.* 122(22), 222101 (2023)
145. M. Cheng, J. Yang, X. Li, H. Li, R. Du, J. Shi, and J. He, Improving the device performances of two-dimensional semiconducting transition metal dichalcogenides: Three strategies, *Front. Phys.* 17(6), 63601 (2022)
146. H. Zeng, Y. Wen, L. Yin, R. Cheng, H. Wang, C. Liu, and J. He, Recent developments in CVD growth and applications of 2D transition metal dichalcogenides, *Front. Phys.* 18(3), 53603 (2023)
147. S. Zeng, F. Li, C. Tan, L. Yang, and Z. Wang, Defect repairing in two-dimensional transition metal dichalcogenides, *Front. Phys.* 18(5), 53604 (2023)
148. R. Yang, J. Fan, and M. Sun, Transition metal dichalcogenides (TMDCs) heterostructures: Optoelectric properties, *Front. Phys.* 17(4), 43202 (2022)